

TRGS-SLAM: IMU-Aided Gaussian Splatting SLAM for Blurry, Rolling Shutter, and Noisy Thermal Images

Spencer Carmichael[†], Katherine A. Skinner
 University of Michigan, Ann Arbor, MI USA
 {specarmi, kskin}@umich.edu

Abstract

Thermal cameras offer several advantages for simultaneous localization and mapping (SLAM) with mobile robots: they provide a passive, low-power solution to operating in darkness, are invariant to rapidly changing or high dynamic range illumination, and can see through fog, dust, and smoke. However, uncooled microbolometer thermal cameras, the only practical option in most robotics applications, suffer from significant motion blur, rolling shutter distortions, and fixed pattern noise. In this paper, we present TRGS-SLAM, a 3D Gaussian Splatting (3DGS) based thermal inertial SLAM system uniquely capable of handling these degradations. To overcome the challenges of thermal data, we introduce a model-aware 3DGS rendering method and several general innovations to 3DGS SLAM, including B-spline trajectory optimization with a two-stage IMU loss, view-diversity-based opacity resetting, and pose drift correction schemes. Our system demonstrates accurate tracking on real-world, fast motion, and high-noise thermal data that causes all other tested SLAM methods to fail. Moreover, through offline refinement of our SLAM results, we demonstrate thermal image restoration competitive with prior work that required ground truth poses. The code is available at: https://umautobots.github.io/trgs_slam.

1. Introduction

The capability of thermal cameras to operate under adverse illumination and see through visual obscurants opens new applications for simultaneous localization and mapping (SLAM) frameworks for mobile robots. A highly motivating example is a thermal camera-equipped robot mapping a dangerous environment, bringing valuable situational awareness to rescue workers [48]. Given the low weight, power consumption, and price of uncooled microbolometer thermal cameras (relative to their cooled counterparts [13, 57]), they are the likely choice in this scenario. However, these

[†]Corresponding author.

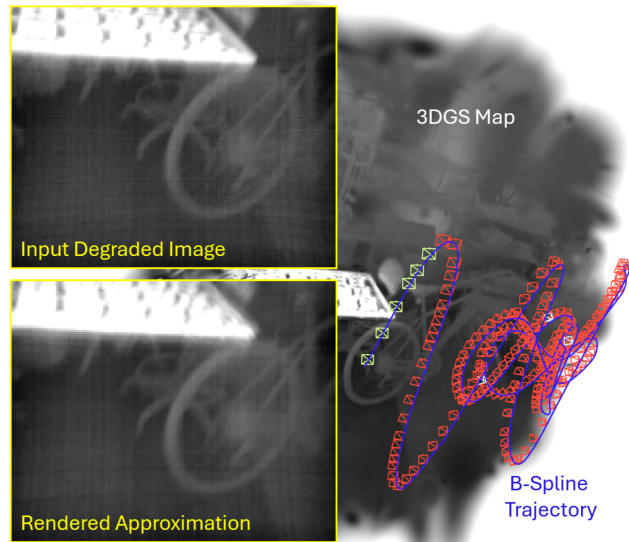


Figure 1. The main elements of TRGS-SLAM. **Left:** Microbolometer-aware rendering. **Right:** 3DGS map and B-spline trajectory.

cameras pose challenges for SLAM. Under slow motion, the low contrast and fixed pattern noise (FPN) of the images are the main issues, and these topics have been well addressed [8, 17, 23, 26, 38, 53, 56, 61]. However, in some scenarios, including the search and rescue context, aggressive camera motion may be necessary. In this case, the images are further afflicted by motion blur and rolling shutter distortions, problems that are seldom addressed in prior work on thermal SLAM.

Recent work, TRNeRF, has demonstrated that given ground truth poses, thermal images with significant FPN, motion blur, and rolling shutter distortions can be restored [7]. This is accomplished by modeling microbolometer degradations within the rendering pipeline of a Neural Radiance Field (NeRF) [32]. Concurrently, in the visual domain, related techniques on motion deblurring with NeRF and 3D Gaussian Splatting (3DGS) [9, 25, 51, 60] have been incorporated in online SLAM systems [1, 14, 52].

In this paper, we extend the ideas of TRNeRF into an on-line 3DGS SLAM system (Fig. 1). This requires significant innovation, as the frontend tracking systems and monocular depth networks relied on by many NeRF and 3DGS SLAM systems are unreliable under the degradations we seek to overcome. Instead, we utilize a B-spline trajectory and tightly fuse with an IMU to estimate and constrain the continuous poses needed to model blur and rolling shutter. We also introduce other general ideas to 3DGS SLAM, including new techniques for opacity resetting and pose drift correction. We demonstrate, with a thorough benchmark on the TRNeRF dataset, that our method is uniquely capable of accurate tracking under severe thermal degradations. In addition, through offline refinement of our SLAM results, we achieve restoration performance comparable to TRNeRF, which utilizes ground truth poses from stereo visual structure from motion.

In summary, our main contributions are as follows:

- A thermal inertial SLAM system, with a 3DGS map and continuous time B-spline trajectory, uniquely capable of accurate tracking under severe image degradation.
- Novel 3DGS SLAM methods, including microbolometer-aware rendering, a two-stage direct IMU loss, view-diversity-based opacity resetting, and pose drift correction schemes.
- A system for offline refinement of the SLAM results that enables thermal image restoration competitive with prior work, but without the need for ground truth poses.

2. Related Work

Thermal SLAM Existing work on thermal SLAM has primarily focused on the low contrast and high noise often present in thermal imagery. Significant effort has been made to identify features robust to these issues: handcrafted features have been exhaustively benchmarked [33, 48, 49], learned features have been trained with FPN-based data augmentation [26, 61], and edge- [8, 17, 53] or line- [23] based features have been investigated. Rather than relying on data association that is invariant to noise, some approaches explicitly estimate and remove FPN online [8, 17, 38, 56]. However, [8] and [17] rely on a bilateral filter to isolate FPN, ignoring its spatially smooth component, while [38] and [56] use the method in [10], which requires pixel correspondences that may be hard to obtain prior to the noise removal (a chicken-and-egg problem, as the authors acknowledge [10]). The method in [10] also estimates FPN only at sparse pixels, interpolating the rest. Our method fits in this latter category, but estimates FPN densely without spatial filtering or correspondences.

It is important to note that thermal cameras also have built-in methods of mitigating FPN. However, shutter-based non-uniformity corrections (NUCs) pose a risk to tracking by pausing the image stream [5], and onboard noise filtering

introduces black-box multi-view inconsistency [7]. To our knowledge, we are the first to investigate this latter issue in SLAM, revealing that onboard filters (often enabled by default) can be very harmful in low contrast scenes.

Despite the susceptibility of microbolometers to motion blur and rolling shutter distortions, these topics have been rarely covered in the thermal SLAM context. While several thermal SLAM papers [11, 12, 20, 21, 36] have applied or built upon ROVIO [3, 4], a blur-robust visual-inertial odometry method, we believe our method is the first to integrate the unique microbolometer model of motion blur. Moreover, to our knowledge, ours is the first thermal SLAM method to consider rolling shutter distortions.

NeRF & 3DGS Restoration NeRF [32] and 3DGS [18] have proven highly effective methods for novel view synthesis and 3D reconstruction. While each originally assumed sharp, global shutter inputs, it has since been demonstrated that accurate NeRF and 3DGS scenes can be trained despite motion blur [9, 25, 51, 60], rolling shutter distortions [27, 55], or a combination of these degradations [7, 41]. In particular, TRNeRF restores highly degraded thermal images by modeling the microbolometer in the NeRF rendering pipeline [7]. We translate this idea into 3DGS, improving efficiency, and extend the FPN parameterization. More importantly, we eliminate TRNeRF’s requirement for ground truth poses by integrating these concepts into a SLAM system.

NeRF & 3DGS SLAM Initially parallel to the work on restoration, NeRF [32] and 3DGS [18] have been increasingly used as dense, high fidelity map representations in SLAM [47]. NeRF and 3DGS SLAM methods can be broadly categorized as frame-to-frame or frame-to-model [47]. Frame-to-frame methods typically employ existing SLAM methods (e.g., ORB-SLAM3 [6] or DROID-SLAM [46]) as frontends, optimizing the NeRF or 3DGS map in the backend. Frame-to-model methods utilize the NeRF or 3DGS map across the entire system, performing tracking directly against the map. As our benchmark suggests (Sec. 4.3), existing frame-to-frame tracking methods struggle with the degradations we target, pointing to the frame-to-model strategy as more promising. Monocular(-inertial) frame-to-model approaches are much fewer in number. Among them, MonoGS [31] stands out from other methods [30, 44, 64] that rely on monocular depth networks (unreliable with degraded thermal images). We therefore draw the most inspiration from MonoGS [31], especially in map initialization, keyframe selection, and Gaussian creation, while also substantially expanding upon it and developing our system from scratch around a different rasterizer (gsplat [58]).

Recently, the lines of research on restoration and SLAM have intersected in multiple papers on blur-aware NeRF-

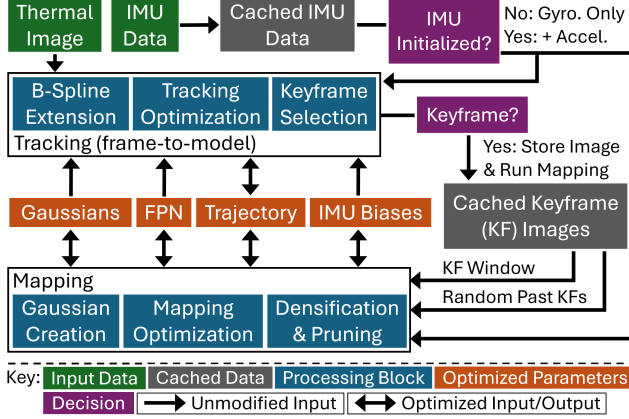


Figure 2. TRGS-SLAM system diagram

and 3DGS-based visual SLAM [1, 14, 52]. However, none fuse with an IMU or utilize a B-spline trajectory, and the monocular demonstrations rely on frame-to-frame tracking [1, 14] and monocular depth estimates [14]. There are also several NeRF and 3DGS SLAM papers that share elements with our system, but do not leverage them to the same extent. TS-SLAM [16] is an RGB-D method that jointly optimizes a B-spline trajectory together with a NeRF map, but uses a dynamics prior rather than fusing with an IMU. [56] proposes a thermal monocular NeRF SLAM method that, like ours, estimates FPN, but does so through pixel correspondences (as noted above). Moreover, it relies on a visual SLAM frontend, DSM [65], that is not blur or rolling shutter-aware. Finally, existing monocular-inertial methods limit the direct influence of the IMU to their frontends [2, 28, 54] or, more narrowly, to initializing the camera pose in tracking [44]. In contrast, we use an IMU loss directly in optimizing the 3DGS map, pivotally including gyroscope data from the beginning.

B-Splines in Rolling Shutter SLAM We draw inspiration from many rolling shutter-aware SLAM methods that have demonstrated the utility of continuous B-spline trajectories [19, 22, 24, 29, 37]. As originally observed in [29], this representation naturally supports estimation of the range of poses contributing to each rolling shutter frame, while also enabling residuals to be computed directly against IMU measurements (without need for IMU (pre-)integration). To support our SLAM method and future work, we contribute a stand-alone package for efficient, on-manifold, B-spline trajectory optimization with Pytorch (detailed in Sec. A¹).

3. Method

Figure 2 presents a high level overview of TRGS-SLAM, highlighting the data and parameters flowing in and out of

¹Supplementary material elements are referred to only by their alphanumeric section labels for brevity

tracking (Sec. 3.5) and mapping (Sec. 3.6). The B-spline and IMU loss (Sec. 3.2) are used throughout the system, as are the 3DGS map and microbolometer-aware rendering method (Sec. 3.3). These components involve the learned IMU biases and FPN, respectively.

3.1. Preliminary: Microbolometer Image Model

In a raw microbolometer thermal image, the value of pixel (x_p, y_p) at time t can be given by [7]:

$$\tilde{n}'_{x_p, y_p}(t) = \tilde{m}'_{x_p, y_p}(t) + \tilde{o}'_{x_p, y_p}(t) \quad (1)$$

$$\tilde{m}'_{x_p, y_p}(t) = \frac{1}{\tau} \int_{-\infty}^t \exp\left(\frac{s-t}{\tau}\right) \tilde{p}'_{x_p, y_p}(s) ds \quad (2)$$

Equation (2) describes the distinct model of motion blur in microbolometers, producing blurry pixel value $\tilde{m}'_{x_p, y_p}(t)$. $\tilde{p}'_{x_p, y_p}(t)$ is a value directly proportional to the power incident on pixel (x_p, y_p) at time t and τ is the camera’s thermal time constant. Equation (1) gives the final pixel value $\tilde{n}'_{x_p, y_p}(t)$, modeling slowly varying FPN as a pixel-wise offset $\tilde{o}'_{x_p, y_p}(t)$. The prime symbol denotes that these are quantities relating to a lens-distorted image and the tilde denotes that these are measured quantities. Additionally, microbolometers employ a rolling shutter readout such that the value of pixel (x_p, y_p) in image l is obtained by evaluating Eq. (1) at time $t'_{x_p, y_p, l}$ [7]:

$$t'_{x_p, y_p, l} = t'_{0,0,l} + x_p \Delta t_{\text{pix}} + y_p w \Delta t_{\text{pix}} \quad (3)$$

where $t'_{0,0,l}$ is the time the top left pixel $(0, 0)$ is read out, Δt_{pix} is the readout delay between each pixel, and w is the width of the image. We refer readers to [7] for more detail.

3.2. B-Spline Trajectory & IMU Loss

We represent the continuous-time trajectory with two uniform B-splines, one for position $\mathbf{p}(t) \in \mathbb{R}^3$ and one for rotation $\mathbf{R}(t) \in \text{SO}(3)$ (as defined in Sec. A.1). The B-splines’ values are determined by control points, \mathbf{p}_i and \mathbf{R}_i , knots, t_i , and the spline order, k . The value of a B-spline at any time t is influenced by k active control points and the trajectory is estimated through their optimization.

The relative scale trajectory of the camera in the world frame will be denoted as $\bar{\mathbf{T}}_C^W(t)$, where the bar indicates the relative scale. Prior to IMU initialization (Sec. 3.7), the position and rotation splines represent this trajectory directly: $\bar{\mathbf{T}}_C^W(t) = [\mathbf{R}_C^W(t), \bar{\mathbf{p}}_C^W(t)]$. After IMU initialization, the position and rotation splines represent the absolute scale trajectory of the IMU, $\mathbf{T}_I^W(t) = [\mathbf{R}_I^W(t), \mathbf{p}_I^W(t)]$, and $\bar{\mathbf{T}}_C^W(t)$ is evaluated using the calibrated IMU extrinsics $\mathbf{T}_C^I(t) = [\mathbf{R}_C^I, \mathbf{p}_C^I]$ and estimated scale factor S :

$$\bar{\mathbf{T}}_C^W(t) = [\mathbf{R}_I^W(t) \mathbf{R}_C^I, \frac{1}{S} (\mathbf{R}_I^W(t) \mathbf{p}_C^I + \mathbf{p}_I^W(t))] \quad (4)$$

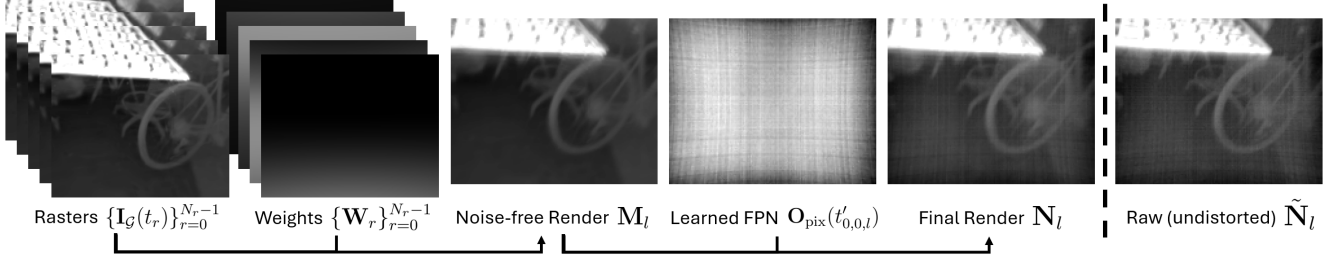


Figure 3. Microbolometer-aware rendering process. A sum of multiple rasters, each multiplied with precomputed pixel-wise weights, is combined with a learned FPN estimate to obtain an approximation of the degraded input image.

B-splines have closed form derivatives and are C^{k-2} continuous (see Sec. A.2 for details). Therefore, $k \geq 4$ ensures continuous acceleration and enables direct comparisons between derivatives of the estimated trajectory and IMU measurements. Prior to IMU initialization, we compute a residual $\mathbf{r}_{g,m}$ against gyroscope measurement $\tilde{\omega}_{1,m}^1$ taken at time t_m as:

$$\mathbf{r}_{g,m} = \mathbf{R}_C^1 \omega_C^C(t_m) - (\tilde{\omega}_{1,m}^1 - \mathbf{b}_g) \quad (5)$$

where $\omega_C^C(t)$ is the estimated angular velocity and \mathbf{b}_g is the gyroscope bias. After IMU initialization, we compute a gyroscope $\mathbf{r}_{g,m}$ and accelerometer $\mathbf{r}_{a,m}$ residual as:

$$\begin{aligned} \mathbf{r}_{g,m} &= \omega_1^1(t_m) - (\tilde{\omega}_{1,m}^1 - \mathbf{b}_g) \\ \mathbf{r}_{a,m} &= \mathbf{a}_1^W(t_m) - (\mathbf{R}_1^W(t_m)(\tilde{\mathbf{a}}_{1,m}^1 - \mathbf{b}_a) + G\hat{\mathbf{g}}^W) \end{aligned} \quad (6)$$

where $\omega_1^1(t)$, $\mathbf{a}_1^W(t)$, and $\mathbf{R}_1^W(t)$ are the estimated angular velocity, linear acceleration, and rotation, $\tilde{\mathbf{a}}_{1,m}^1$ is an accelerometer measurement taken at time t_m , \mathbf{b}_a is the accelerometer bias, $\hat{\mathbf{g}}^W$ is the direction of gravity in the world frame (as a unit vector), and G is the magnitude of gravity. Note that \mathbf{b}_g and \mathbf{b}_a are learned parameters, while $\hat{\mathbf{g}}^W$ is held constant outside of periodic updates (Sec. 3.7).

Given a set of IMU measurements \mathcal{I} we compute an IMU-based loss $\mathcal{L}_{\text{IMU},\mathcal{I}}$ as follows:

$$\mathcal{L}_{\text{IMU},\mathcal{I}} = \sum_{m \in \mathcal{I}} \lambda_g \|\mathbf{r}_{g,m}\|_2 + \lambda_a \|\mathbf{r}_{a,m}\|_2 \quad (7)$$

where λ_g and λ_a are scalar coefficients. Note that the terms involving the accelerometer are excluded prior to IMU initialization. Additionally, we compute a loss from the learned biases using another set coefficient λ_{bias} :

$$\mathcal{L}_{\text{bias}} = \lambda_{\text{bias}} (\|\mathbf{b}_g\|_2 + \|\mathbf{b}_a\|_2) \quad (8)$$

to prevent overfitting with outlier residuals.

3.3. 3DGS Map & Microbolometer-Aware Rendering

We represent the map as a set of 3D Gaussians \mathcal{G} , each defined by a scalar opacity σ_g and intensity c_g , and a relative

scale 3D covariance ellipsoid parameterized by a mean $\bar{\mu}_g$, scale \bar{s}_g , and quaternion \mathbf{q}_g in the world frame. In the original 3DGS method [18], spherical harmonics are used to represent view-dependent color. Here, we assume no view dependency to reduce the number of learnable parameters, and we require only a scalar intensity as thermal images are single-channel.

In 3DGS [18], images are rasterized by splatting (projecting) the 3D Gaussians onto the 2D image plane and computing a pixel value p as:

$$p = \sum_{g \in \mathcal{B}} c_g \alpha_g \prod_{j=1}^{g-1} (1 - \alpha_j) \quad (9)$$

where \mathcal{B} is a depth-ordered subset of Gaussians visible to the pixel and α_g is obtained by multiplying the Gaussian's opacity σ_g by the Gaussian's 2D distribution evaluated at the pixel coordinate. The primary inputs to the 3DGS method are a set of sharp, global shutter images $\{\tilde{\mathbf{I}}_l\}_{l=0}^{N_{\text{img}}-1}$ and corresponding camera pose estimates $\{\tilde{\mathbf{T}}_{C,l}^W\}_{l=0}^{N_{\text{img}}-1}$. The 3D to 2D projection assumes an ideal pinhole camera model, so lens undistortion is applied to the input images to obtain $\{\tilde{\mathbf{I}}_l\}_{l=0}^{N_{\text{img}}-1}$. In training, the loss is computed by rasterizing an image $\mathbf{I}_{G,l}$ at pose $\tilde{\mathbf{T}}_{C,l}^W$ and directly comparing it to $\tilde{\mathbf{I}}_l$. To adapt this to degraded thermal images, we extend the rendering pipeline to rasterize multiple images, blend them together, and sum the result with learned FPN.

Let $[\tilde{\mathbf{N}}_l]_{y_p, x_p} = \tilde{n}_{x_p, y_p}(t_{x_p, y_p, l})$ denote a raw microbolometer image after downsampling and lens undistortion. We show in Sec. B that $\tilde{n}_{x_p, y_p}(t_{x_p, y_p, l})$ approximately follows the form of Eq. (1) at an effective readout time $t_{x_p, y_p, l}$. To render an estimate of $\tilde{\mathbf{N}}_l$, we begin by computing $[\mathbf{M}_l]_{y_p, x_p} = m_{x_p, y_p}(t_{x_p, y_p, l})$. To do this, we rasterize N_r images at times $\{t_r\}_{r=0}^{N_r-1}$ evenly spaced over $[t_{\text{max},l} - T_b, t_{\text{max},l}]$, where $t_{\text{max},l}$ is the latest effective readout time across $\tilde{\mathbf{N}}_l$, and T_b is the maximum integration interval. This rasterization involves evaluating the position and rotation splines at each time to obtain $\{\tilde{\mathbf{T}}_C^W(t_r)\}_{r=0}^{N_r-1}$. Treating the pixel values of the rasterized images $\{\mathbf{I}_G(t_r)\}_{r=0}^{N_r-1}$ as samples $\{p_{x_p, y_p}(t_r)\}_{r=0}^{N_r-1}$, we can compute $m_{x_p, y_p}(t_{x_p, y_p, l})$ as a discrete integral in the form

of Eq. (2). Ultimately, as detailed in Sec. C, the computation of \mathbf{M}_l can be efficiently cast as a sum of element-wise products:

$$\mathbf{M}_l = \sum_{r=0}^{N_r-1} \mathbf{I}_G(t_r) \odot \mathbf{W}_r \quad (10)$$

where $\{\mathbf{W}_r\}_{r=0}^{N_r-1}$ are precomputed weights that are a function of $N_r, T_b, \tau, \Delta t_{\text{pix}}$, and the lens undistortion maps.

To model the slowly time varying FPN, we use two splines: $\mathbf{O}_{\text{pix}}(t) \in \mathbb{R}^{h \times w}$ and $o_{\text{global}}(t) \in \mathbb{R}$, where w and h are the image width and height, respectively. $\mathbf{O}_{\text{pix}}(t)$ models pixel-wise FPN and, similar to TRNeRF [7], we use the following loss to encourage $\mathbf{O}_{\text{pix}}(t)$ to be zero-mean:

$$\mathcal{L}_{\text{FPN}}(t) = \frac{\lambda_{\text{FPN}}}{wh} \left| \sum_{x_p=0}^{w-1} \sum_{y_p=0}^{h-1} [\mathbf{O}_{\text{pix}}(t)]_{y_p, x_p} \right| \quad (11)$$

where λ_{FPN} is a set coefficient. As $\mathbf{O}_{\text{pix}}(t)$ is zero-mean, we use $o_{\text{global}}(t)$ to separately account for global (image-wide) intensity changes. Both of these splines are constructed similarly to the position spline (see Sec. A.1). The control points of $\mathbf{O}_{\text{pix}}(t)$ are stored as vectors in \mathbb{R}^{wh} and the result of evaluating the spline is reshaped. Note that the spline knot intervals can be used to independently control how slowly these FPN components vary.

Putting these parts together, the final render for image N_l is computed as follows:

$$\mathbf{N}_l = \mathbf{M}_l + \mathbf{O}_{\text{pix}}(t'_{0,0,l}) + o_{\text{global}}(t'_{0,0,l}) \quad (12)$$

The process is visualized in Fig. 3. We define the loss for image l as the mean absolute error between the rendered image and the undistorted image:

$$\mathcal{L}_{\text{img},l} = \frac{1}{wh} \|\mathbf{N}_l - \tilde{\mathbf{N}}_l\|_1 \quad (13)$$

3.4. System Initialization

The position and rotation splines are initialized with all control points set to zero and identity, respectively (i.e., the initial camera frame defines the world frame). All control points of both FPN splines are also initialized to zero. The map is initialized as a plane of N_{init} Gaussians one unit (unscaled) in front of the camera. This is done by randomly sampling N_{init} pixels across the first image. The Gaussian means are initialized by back projecting the pixels with a depth of 1 and the pixel values are used to set the intensities. The opacities are set to a default value, the quaternions are randomized, and the scale of each Gaussian is set to the average distance of its three nearest neighbors. The Gaussians are subsequently fit to the first image through $N_{\text{iter,init}}$ iterations of optimization with the following loss:

$$\mathcal{L}_{\text{init}} = \frac{1}{wh} \|\mathbf{I}_G(t'_{0,0,0}) - \tilde{\mathbf{N}}_0\|_1 \quad (14)$$

Note that at this stage only the Gaussians are optimized and blur and rolling shutter are not yet modeled. For stability, blur and rolling shutter are not modeled until after a set number of initial keyframes.

3.5. Tracking

After initialization, tracking is applied to each new image.

B-Spline Extension The splines can be evaluated for $t \in [t_0, t_0 + (N_c - k + 1)\Delta t_c]$, where N_c is the total number of control points and Δt_c is the knot interval. When a new image l arrives, control points must be added to extend the splines to the end of readout $t_{\text{max},l}$ prior to tracking optimization. In the early stages of our system, this is done by simply duplicating the last control point of each spline. After a set number of keyframes, we additionally compute N_q predicted poses at times $\{t_q\}_{q=0}^{N_q-1}$ evenly spaced over $[t'_{0,0,l-1}, t_{\text{max},l}]$ and fit the active set of control points to these predictions. Prior to IMU initialization, predictions are made assuming constant velocity; after IMU initialization, predictions are made through IMU integration. Further details on this process are provided in Sec. A.5. The FPN splines, $\mathbf{O}_{\text{pix}}(t)$ and $o_{\text{global}}(t)$, must also be extended occasionally. When necessary, we extend the FPN splines by duplicating their last control points, without fitting them to any predictions.

Tracking Optimization In tracking we optimize the position and rotation control points only. All other parameters are frozen. Optimization is performed for a maximum of $N_{\text{iter,track}}$ iterations with the following loss:

$$\mathcal{L}_{\text{track}} = \frac{1}{|\mathcal{I}_{\text{track}}|} \mathcal{L}_{\text{IMU}, \mathcal{I}_{\text{track}}} + \mathcal{L}_{\text{img},l} \quad (15)$$

where $\mathcal{I}_{\text{track}}$ is the set of IMU measurements taken over $[\min(t_{0,0,l-1}, t_{\text{max},l} - T_b), t_{\text{max},l}]$. Optimization is considered converged if the average change in both the positions and rotations across the raster timestamps falls below set thresholds.

Keyframe Selection & Window Management After tracking optimization, we follow MonoGS [31] and select the current image as a keyframe if it satisfies one of two conditions: the translation since the last keyframe (normalized by the relative scale median depth) exceeds a threshold, or the intersection over union between the currently visible Gaussians and those visible to the last keyframe falls beneath a threshold. Unlike MonoGS, our keyframe window is defined simply as the last N_{window} keyframes. We have found that the random keyframe sampling in mapping is sufficient to provide wide-baseline multi-view constraints.

3.6. Mapping

When a new keyframe is selected, mapping is applied.

Gaussian Creation Prior to mapping optimization, new Gaussians are created by randomly sampling and back projecting pixels in the new keyframe, as done with the first image in Sec. 3.4. However, in this case, the depth of new Gaussians is set to the relative scale median depth in the new keyframe, and the sampling is restricted to pixels with an accumulated alpha value beneath a set threshold (where the accumulated alpha value is given by Eq. (9) with c_g removed). The number of new Gaussians is set as $N_{\max} N_{\text{cand}}/(wh)$ where N_{\max} is a set parameter and N_{cand} is the number of candidate pixels (as determined by the alpha threshold). This avoids creating new Gaussians in previously mapped areas.

Mapping Optimization In mapping we jointly optimize all learned parameters: the IMU biases, the Gaussians, and the position, rotation, and FPN control points. Optimization is performed for $N_{\text{iter,map}}$ iterations with the following loss:

$$\mathcal{L}_{\text{map}} = \frac{1}{|\mathcal{I}_{\text{map}}|} (\lambda_w \mathcal{L}_{\text{IMU}, \mathcal{W}_K} + \lambda_s \mathcal{L}_{\text{IMU}, \mathcal{S}_K}) + \mathcal{L}_{\text{bias}} + \frac{1}{|\mathcal{K}|} \left(\lambda_w \sum_{l \in \mathcal{W}_K} \mathcal{L}_{\text{img}, l} + \lambda_s \sum_{l \in \mathcal{S}_K} \mathcal{L}_{\text{img}, l} + \sum_{l \in \mathcal{K}} \mathcal{L}_{\text{FPN}}(t'_{0,0,l}) \right) \quad (16)$$

where \mathcal{W}_K is the set of all keyframes in the current window, \mathcal{S}_K is a set of past keyframes randomly sampled at each iteration, and $\mathcal{K} = \mathcal{W}_K \cup \mathcal{S}_K$. \mathcal{W}_I and \mathcal{S}_I are disjoint sets of IMU measurements associated with \mathcal{W}_K and \mathcal{S}_K , and $\mathcal{I}_{\text{map}} = \mathcal{W}_I \cup \mathcal{S}_I$. The coefficients λ_w and λ_s balance the influence of the keyframe window relative to the past keyframes. Without these coefficients, we observed that pose drift was not consistently corrected. Rather, the keyframe window frequently overwrote previously observed portions of the map. We address this by setting $\lambda_s > \lambda_w$ to give more weight to the past keyframes. The coefficients are applied to both the image and the IMU losses to maintain balance between them. Additionally, we manually modify the gradients of the trajectory control points and Gaussians to compensate for this weighting scheme. The full details are given in Sec. D.

View-Diversity-Based Opacity Resetting The original 3DGS paper [18] introduces several rules that are periodically applied to split, duplicate, prune, and reset Gaussians. These rules serve to populate empty areas and reconstruct detail. One such rule, intended to reduce the number of Gaussians, is to periodically reset the Gaussian opacities to a low value. In combination with a rule to prune low opacity Gaussians, this allows subsequent optimization to recover necessary Gaussians only and cull the rest. However, this global resetting is inefficient and destabilizing in the SLAM context. Therefore, we limit this resetting to Gaussians with poor view diversity. Specifically, at each mapping iteration

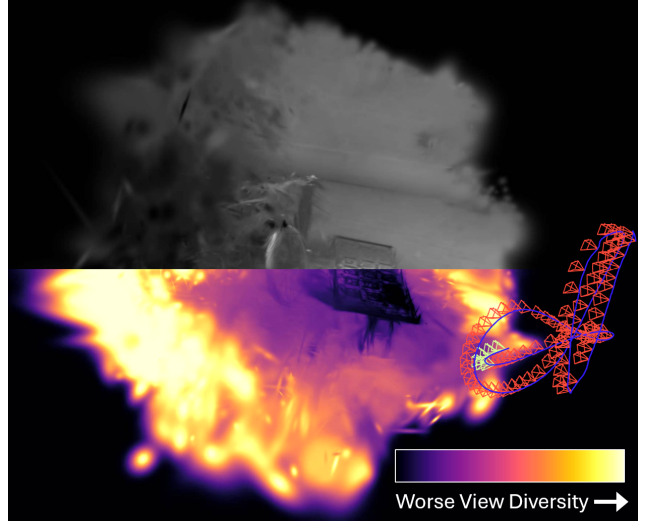


Figure 4. A depiction of the Gaussians targeted by our view-diversity-based opacity resetting. The color scale is mapped to the log of the condition number of \mathbf{V}_g for each Gaussian.

we compute the following for each Gaussian g :

$$\mathbf{V}_g = \mathbf{V}_{g,\text{prev}} + \sum_{r \in \mathcal{R}_g} \hat{\mathbf{d}}_{r,g} \hat{\mathbf{d}}_{r,g}^T \quad (17)$$

where $\mathbf{V}_{g,\text{prev}}$ is the result from the previous iteration, \mathcal{R}_g is the subset of rasters the Gaussian appears in, and $\hat{\mathbf{d}}_{r,g}$ is the unit vector pointing from the camera center at raster r to the Gaussian mean $\bar{\boldsymbol{\mu}}_g$. \mathbf{V}_g is therefore the second moment matrix of these view directions, accumulated over many mapping iterations. When it comes time to reset opacities, we compute the condition number of each \mathbf{V}_g and reset Gaussians with a condition number above a set threshold. \mathbf{V}_g is then reset to $\mathbf{0}$. As shown in Fig. 4, this tends to eliminate poorly constrained Gaussians at the edges of the scene.

We maintain the remaining rules for splitting, duplicating, and pruning. However, as detailed in Sec. E, the gradient accumulation involved in these rules must be modified to accommodate our microbolometer-aware rendering. When the rules are applied, the mapping iteration counter is reset to ensure the map is stable before tracking resumes.

Relocalization When the current keyframe image l observes a new area, mapping is largely unconstrained and consistently results in a high SSIM value between the noise-free render \mathbf{M}_l and denoised input image $\tilde{\mathbf{N}}_l - \mathbf{O}_{\text{pix}}(t'_{0,0,l}) - o_{\text{global}}(t'_{0,0,l})$. The SSIM is also high when the camera is accurately localized in a pre-existing portion of the map. However, given that the weighting scheme in Eq. (16) prevents overwriting, mapping can fail to fit the Gaussians to the current keyframe image when a part of the scene is re-observed after significant drift. Therefore, low SSIM signals

tracking failure. We implement a simple scheme to recover from tracking failure. When the SSIM is below a set threshold after mapping, we revert the full system state to before mapping and resume tracking. This effectively pauses mapping until tracking is able to relocalize. During this phase, we reduce the IMU residual coefficients, λ_g and λ_a , to allow pose optimization to temporarily ignore dynamics and jump to the correct solution.

3.7. IMU Initialization & Updates

IMU initialization solves for the unknown gravity direction \hat{g} and scale factor S needed to compute a loss against the accelerometer. It also produces an estimate of the gyroscope and accelerometer biases, \mathbf{b}_g and \mathbf{b}_a . After a set period, we perform IMU initialization as described in [66] using keyframe poses sampled at a set rate and all IMU measurements. Using the estimated scale factor, we transform the trajectory to the IMU frame with absolute scale. To smooth the trajectory, we run mapping optimization for set number of iterations with two changes: we use all IMU measurements at each iteration and all keyframes are randomly sampled. As the initial scale estimate can be poor, we periodically rerun the method in [66] to update the scale and gravity direction. Full details on the application of scale updates are provided in Sec. F.

3.8. Offline Refinement

We perform offline refinement of the SLAM results by running a set number of additional mapping iterations using all IMU data at each iteration and randomly sampling from all frames (not just keyframes). In this process, we operate on the full resolution images, increase the number of rasters per render, introduce the gravity direction unit vector as an additional learned parameter, drop the IMU bias loss, and re-introduce global opacity resetting.

4. Experiments

4.1. Dataset

We evaluate our method’s SLAM and restoration performance on the TRNeRF dataset [7]. This dataset includes six sequences combining three camera speeds (slow, medium, and fast) with two scenes (indoor and outdoor). We refer to these sequences by the first letter of the speed and scene (e.g., SO denotes slow outdoor). These combinations allow for an isolation of variables: blur and rolling shutter are insignificant in the slow sequences, and FPN is most prominent in the low contrast indoor scene. See Sec. G for further details.

4.2. Implementation

We build TRGS-SLAM in PyTorch. For simplicity, the system uses a single process (tracking waits for mapping). We use the gsplat 3DGS library [58] to benefit from its

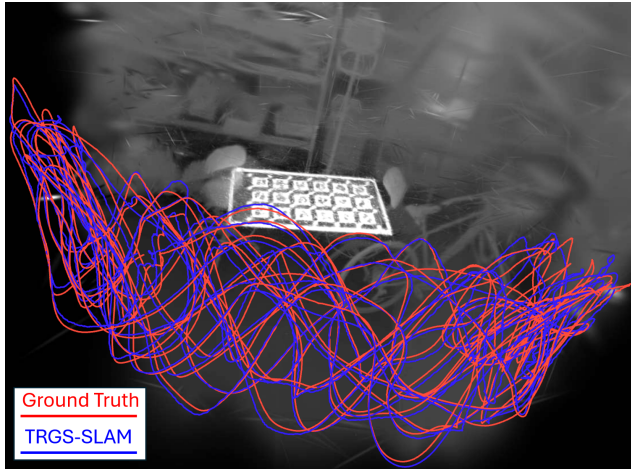


Figure 5. TRGS-SLAM result on the medium indoor sequence.

Table 1. RMSE ATE in cm on the TRNeRF dataset.

Type	Method	SO	MO	FO	SI	MI	FI
Monocular	ORB-SLAM3	0.8	9.4	×	×	×	×
	DSM	9.4	×	×	76.7	×	×
	DROID-SLAM	0.5	2.6	×	0.7	×	×
	MASt3R-SLAM*	1.6	94.5	×	2.7	88.4	×
	MonoGS	7.7	×	×	83.9	×	×
Mono-Inertial	ORB-SLAM3 (inertial)	1.1	×	×	×	×	×
	DM-VIO	1.5	44.2	×	25.2	×	×
	DBA-VIO	1.4	25.2	×	2.5	26.5	×
	ROTIO	18.5	53.2	×	37.1	×	×
	TRGS-SLAM	12.7	5.5	2.4	6.4	3.9	4.2

* RMSE ATE and alignment performed with keyframes only.

× program exited early or error exceeded 1 meter.

efficient batched rasterization, camera pose gradients, and implementation of anti-aliasing [59]. We reimplement the IMU initialization method of [66] in Python. We introduce a standalone package for B-spline optimization that uses the algorithms introduced in [42], and the software libraries PyPose [50] and LieTorch [45], to achieve efficient and stable on-manifold optimization (detailed in Sec. A). As performed in [7], we rescale the 16-bit thermal images into the $[0, 1]$ range using predefined thresholds. Here, we use the 0.5 and 99.5 percentiles of the pixel values observed in each sequence. We otherwise run TRGS-SLAM with the same parameters across all sequences, detailed fully in Sec. H.

4.3. SLAM Evaluation

We compare TRGS-SLAM against a variety of visual and thermal SLAM methods. To make the case for the frame-to-model paradigm, we test several methods used as frontends in frame-to-frame systems: ORB-SLAM3 [6], DROID-SLAM [46], DSM [65], and DBA-VIO [62] (an inertial extension of DROID-SLAM). We also include the frame-to-model system MonoGS [31], the direct visual inertial method DM-VIO [43], and the paradigm-shifting MASt3R-SLAM [34] (based on two-view reconstruction priors). Although few thermal SLAM methods are publicly available, we are

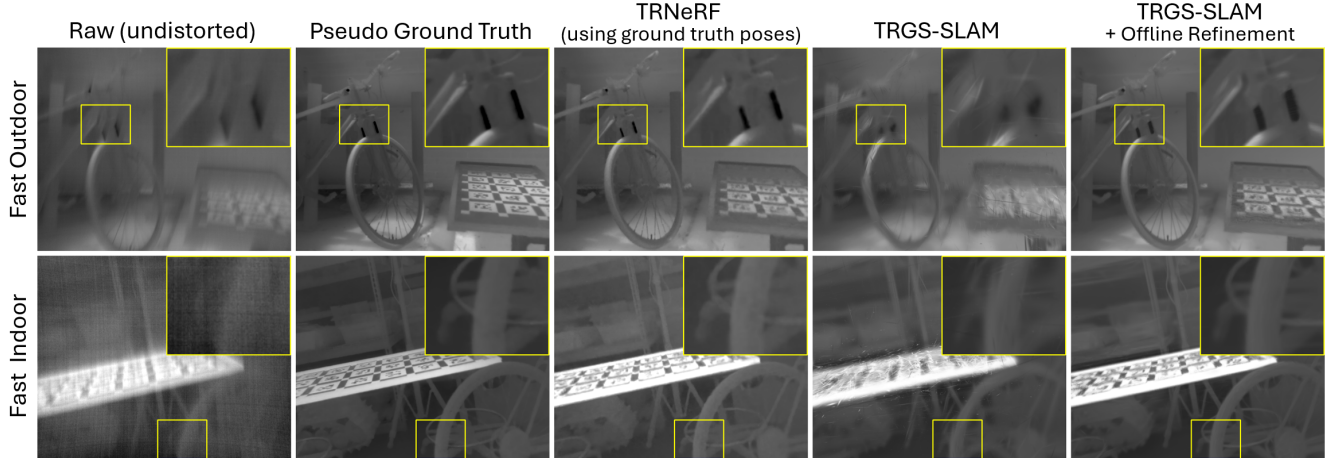


Figure 6. Qualitative restoration results. With offline refinement, TRGS-SLAM achieves restoration quality near that of TRNeRF.

able to test ROTIO [20] (using the implementation of [12]), a 16-bit adaptation of ROVIO [3, 4]. With the exception of ROTIO, we rescale the input images with the same thresholds used in our method (and convert to 8-bit), but run on the full resolution images (barring standard resizing procedures [34, 46, 62]). For each sequence, we report the average RMSE ATE across three trials, using Sim(3) alignment in the pure monocular case and SE(3) alignment otherwise (using [15]). Unless otherwise noted, the alignment and RMSE ATE calculation are performed using all frames.

Table 1 gives the results. In the SO sequence, where degradation is nearly absent, TRGS-SLAM is outperformed by multiple baselines. In part, this is due to scale error (our result is 4.7 cm with Sim(3) alignment). The slow motion makes IMU initialization difficult, though the performance of other inertial methods suggests this aspect of our system could be improved. The value of our method is apparent in the remaining sequences. While some baselines demonstrate impressive robustness under moderate degradation (MO and SI), ours is the only method capable of accurate tracking in the most challenging sequences (FO, MI, and FI). Our result on the MI sequence is shown in Fig. 5.

A thorough ablation study is presented in Sec. I. The results confirm that to obtain good performance on all sequences it is necessary to use gyroscope data immediately, model all degradations, employ our pose drift corrections schemes, and perform view-diversity-based opacity resetting. Additionally, it is shown that onboard camera noise filters can severely harm performance in the indoor scene.

4.4. Restoration Evaluation

We compare the restoration performance of TRGS-SLAM in combination with offline refinement (Sec. 3.8) against TRNeRF [7] and the best performing baseline from that paper, GS on the Move [41] (both using ground truth poses). The parameters used for offline refinement are given in Sec. H.

Table 2. LPIPS results on the TRNeRF dataset (lower is better)

Method	MO	FO	MI	FI
GS on the Move*	0.093	0.283	0.206	0.328
TRNeRF*	0.042	0.078	0.068	0.117
TRGS-SLAM + Refinement	0.067	0.098	0.095	0.116

*Utilize ground truth poses. Results copied from [7].

The LPIPS results are given in Tab. 2 and qualitative results are shown in Fig. 6. Remarkably, the results are competitive with TRNeRF, even marginally outperforming it on the FI sequence.

4.5. Timing & Memory Analysis

With a NVIDIA RTX A6000 GPU and an AMD Ryzen 9 5950X CPU, tracking runs at 5-7 Hz and mapping takes 1.3-1.6 seconds per keyframe. Due to the variable frequency of keyframe generation, this leads to an overall FPS of 1-4, with the lowest FPS in the fast sequences. While similar to MonoGS [31], this FPS falls well short of real time operation with fast motion. More timing information and a broader discussion of limitations are provided in Sec. J and Sec. K, respectively. Owing to our Gaussians' scalar intensities (rather than RGB or spherical harmonic values) and our opacity resetting strategy (which limits the total number of Gaussians to $\sim 20k-40k$), our system consumes a low amount of memory, peaking at 423 MiB of allocated GPU memory across all SLAM runs.

5. Conclusion

We introduce a thermal inertial SLAM system uniquely capable of accurate tracking on severely degraded images and of supporting, through offline refinement, high quality image restoration without known poses. This robustness is achieved by combining a 3DGS map and microbolometer-aware rendering method with a continuous B-spline trajectory and tight IMU fusion. One future direction is the

extension to large-scale scenes through degradation aware place recognition and loop closure. Future work could also assess the long-term capability of FPN estimation, and whether shutter-based NUCs can be avoided. Additionally, our method could be applied to rolling shutter visible spectrum cameras, with many of the core elements retained.

References

- [1] Gwangtak Bae, Changwoon Choi, Hyeongjun Heo, Sang Min Kim, and Young Min Kim. I2-SLAM: Inverting imaging process for robust photorealistic dense slam. In *European Conference on Computer Vision*, pages 72–89, 2024. 1, 3
- [2] Yucheng Bai. A real-time visual-inertial slam with neural radiance fields mapping. In *Proceedings of the 3rd International Conference on Computer, Artificial Intelligence and Control Engineering*, pages 514–523, 2024. 3
- [3] Michael Bloesch, Sammy Omari, Marco Hutter, and Roland Siegwart. Robust visual inertial odometry using a direct EKF-based approach. In *2015 IEEE/RSJ International Conference on Intelligent Robots and Systems (IROS)*, pages 298–304, 2015. 2, 8
- [4] Michael Bloesch, Michael Burri, Sammy Omari, Marco Hutter, and Roland Siegwart. Iterated extended Kalman filter based visual-inertial odometry using direct photometric feedback. *The International Journal of Robotics Research*, 36(10):1053–1072, 2017. 2, 8
- [5] Paulo Vinicius Koerich Borges and Stephen Vidas. Practical infrared visual odometry. *IEEE Transactions on Intelligent Transportation Systems*, 17(8):2205–2213, 2016. 2
- [6] Carlos Campos, Richard Elvira, Juan J. Gómez Rodríguez, José M. M. Montiel, and Juan D. Tardós. ORB-SLAM3: An accurate open-source library for visual, visual-inertial, and multimap SLAM. *IEEE Transactions on Robotics*, 37(6):1874–1890, 2021. 2, 7
- [7] Spencer Carmichael, Manohar Bhat, Mani Ramanagopal, Austin Buchan, Ram Vasudevan, and Katherine A. Skinner. TRNeRF: Restoring blurry, rolling shutter, and noisy thermal images with neural radiance fields. In *2025 IEEE/CVF Winter Conference on Applications of Computer Vision (WACV)*, pages 7980–7990, 2025. 1, 2, 3, 5, 7, 8, 9
- [8] Jie Chen, Pengshuai Hou, Haoyu Zhao, Zhendong Cao, and Jie Zhao. Eamt-slam: edge-aided monocular thermal sensor slam in low-illumination environments. *IEEE Sensors Journal*, 2024. 1, 2
- [9] Wenbo Chen and Ligang Liu. Deblur-GS: 3D Gaussian Splatting from Camera Motion Blurred Images. *Proceedings of the ACM on Computer Graphics and Interactive Techniques*, 7(1):1–15, 2024. 1, 2
- [10] Manash Pratim Das, Larry Matthies, and Shreyansh Daftry. Online photometric calibration of automatic gain thermal infrared cameras. *IEEE Robotics and Automation Letters*, 6(2):2453–2460, 2021. 2
- [11] Christopher Doer and Gert F. Trommer. Radar Visual Inertial Odometry and Radar Thermal Inertial Odometry: Robust Navigation even in Challenging Visual Conditions. In *2021 IEEE/RSJ International Conference on Intelligent Robots and Systems (IROS)*, pages 331–338, 2021. ISSN: 2153-0866. 2
- [12] Henrik Dobbe Flemmen. Rovtio: Robust visual thermal inertial odometry. Master’s thesis, NTNU, 2021. 2, 8
- [13] Rikke Gade and Thomas B. Moeslund. Thermal cameras and applications: a survey. *Machine Vision and Applications*, 25(1):245–262, 2014. 1
- [14] Francesco Girlanda, Denys Rozumnyi, Marc Pollefeys, and Martin R Oswald. Deblur gaussian splatting slam. *arXiv preprint arXiv:2503.12572*, 2025. 1, 3
- [15] Michael Grupp. evo: Python package for the evaluation of odometry and slam. <https://github.com/MichaelGrupp/evo>, 2017. 8
- [16] Yicheng He, Guangcheng Chen, and Hong Zhang. Optimizing nerf-based slam with trajectory smoothness constraints. In *2025 IEEE International Conference on Robotics and Automation (ICRA)*, pages 11054–11060, 2025. 3
- [17] Pengshuai Hou, Jie Chen, Yule Shao, Xingquan Chen, and Xuehe Zhang. Robust thermal-inertial slam with online photometric calibration and point-edge flow tracking. *Measurement Science and Technology*, 36(8):086308, 2025. 1, 2
- [18] Bernhard Kerbl, Georgios Kopanas, Thomas Leimkuehler, and George Drettakis. 3D Gaussian Splatting for Real-Time Radiance Field Rendering. *ACM Transactions on Graphics*, 42(4):1–14, 2023. 2, 4, 6
- [19] Christian Kerl, Jorg Stuckler, and Daniel Cremers. Dense continuous-time tracking and mapping with rolling shutter rgb-d cameras. In *Proceedings of the IEEE international conference on computer vision*, pages 2264–2272, 2015. 3
- [20] Shehryar Khattak, Frank Mascarich, Tung Dang, Christos Papachristos, and Kostas Alexis. Robust Thermal-Inertial Localization for Aerial Robots: A Case for Direct Methods. In *2019 International Conference on Unmanned Aircraft Systems (ICUAS)*, pages 1061–1068, 2019. 2, 8
- [21] Shehryar Khattak, Huan Nguyen, Frank Mascarich, Tung Dang, and Kostas Alexis. Complementary multi-modal sensor fusion for resilient robot pose estimation in subterranean environments. In *2020 International Conference on Unmanned Aircraft Systems (ICUAS)*, pages 1024–1029, 2020. 2
- [22] Jae-Hak Kim, Cesar Cadena, and Ian Reid. Direct semi-dense slam for rolling shutter cameras. In *2016 IEEE International Conference on Robotics and Automation (ICRA)*, pages 1308–1315, 2016. 3
- [23] Luguang Lai, Linyang Li, Yuxuan Zhou, Letian Zhang, and Dongqing Zhao. TPL-SLAM: Real-Time Monocular Thermal-Inertial SLAM With Point-Line Tracked by Optical Flow. *IEEE Sensors Journal*, pages 1–1, 2025. 1, 2
- [24] Xiaolei Lang, Jiajun Lv, Jianxin Huang, Yukai Ma, Yong Liu, and Xingxing Zuo. Ctrl-VIO: Continuous-time visual-inertial odometry for rolling shutter cameras. *IEEE Robotics and Automation Letters*, 7(4):11537–11544, 2022. 3
- [25] Dongwoo Lee, Jeongtaek Oh, Jaesung Rim, Sunghyun Cho, and Kyoung Mu Lee. Exblurf: Efficient radiance fields for extreme motion blurred images. In *Proceedings of the IEEE/CVF International Conference on Computer Vision*, pages 17639–17648, 2023. 1, 2

- [26] Junwoon Lee, Taisei Ando, Mitsuru Shinozaki, Toshihiro Kitajima, Qi An, and Atsushi Yamashita. Self-tio: Thermal-inertial odometry via self-supervised 16-bit feature extractor and tracker. *IEEE Robotics and Automation Letters*, 2024. 1, 2
- [27] Moyang Li, Peng Wang, Lingzhe Zhao, Bangyan Liao, and Peidong Liu. Usb-nerf: Unrolling shutter bundle adjusted neural radiance fields. In *International Conference on Representation Learning*, pages 55719–55739, 2024. 2
- [28] Daoqing Liao and Wei Ai. Vi-nerf-slam: a real-time visual-inertial slam with nerf mapping. *Journal of Real-Time Image Processing*, 21(2):30, 2024. 3
- [29] Steven Lovegrove, Alonso Patron-Perez, and Gabe Sibley. Spline Fusion: A continuous-time representation for visual-inertial fusion with application to rolling shutter cameras. In *Proceedings of the British Machine Vision Conference 2013*, pages 93.1–93.11, 2013. 3
- [30] Mostafa Mansour, Ahmed Abdelsalam, Ari Happonen, Jari Porras, and Esa Rahtu. Udgs-slam: Unidepth assisted gaussian splatting for monocular slam. *Array*, page 100400, 2025. 2
- [31] Hidenobu Matsuki, Riku Murai, Paul H. J. Kelly, and Andrew J. Davison. Gaussian Splatting SLAM. In *Proceedings of the IEEE/CVF Conference on Computer Vision and Pattern Recognition*, 2024. 2, 5, 7, 8
- [32] Ben Mildenhall, Pratul P Srinivasan, Matthew Tancik, Jonathan T Barron, Ravi Ramamoorthi, and Ren Ng. Nerf: Representing scenes as neural radiance fields for view synthesis. *Communications of the ACM*, 65(1):99–106, 2021. 1, 2
- [33] Tarek Mouats, Nabil Aouf, David Nam, and Stephen Vidas. Performance Evaluation of Feature Detectors and Descriptors Beyond the Visible. *Journal of Intelligent & Robotic Systems*, 92(1):33–63, 2018. 2
- [34] Riku Murai, Eric Dexheimer, and Andrew J Davison. Mast3r-slam: Real-time dense slam with 3d reconstruction priors. In *Proceedings of the Computer Vision and Pattern Recognition Conference*, pages 16695–16705, 2025. 7, 8
- [35] Linfei Pan, Dániel Baráth, Marc Pollefeys, and Johannes L Schönberger. Global structure-from-motion revisited. In *European Conference on Computer Vision*, pages 58–77, 2024. 7
- [36] Christos Papachristos, Frank Mascarich, and Kostas Alexis. Thermal-inertial localization for autonomous navigation of aerial robots through obscurants. In *2018 International Conference on Unmanned Aircraft Systems (ICUAS)*, pages 394–399, 2018. 2
- [37] Alonso Patron-Perez, Steven Lovegrove, and Gabe Sibley. A Spline-Based Trajectory Representation for Sensor Fusion and Rolling Shutter Cameras. *International Journal of Computer Vision*, 113(3):208–219, 2015. 3
- [38] Vincenzo Polizzi, Robert Hewitt, Javier Hidalgo-Carrió, Jeff Delaune, and Davide Scaramuzza. Data-efficient collaborative decentralized thermal-inertial odometry. *IEEE Robotics and Automation Letters*, 7(4):10681–10688, 2022. 1, 2
- [39] Paul-Edouard Sarlin, Cesar Cadena, Roland Siegwart, and Marcin Dymczyk. From Coarse to Fine: Robust Hierarchical Localization at Large Scale. In *2019 IEEE/CVF Conference on Computer Vision and Pattern Recognition (CVPR)*, pages 12708–12717, 2019. 7
- [40] Johannes L. Schonberger and Jan-Michael Frahm. Structure-from-Motion Revisited. In *2016 IEEE Conference on Computer Vision and Pattern Recognition (CVPR)*, pages 4104–4113, 2016. 7
- [41] Otto Seiskari, Jerry Ylilammi, Valtteri Kaatrasalo, Pekka Rantalankila, Matias Turkulainen, Juho Kannala, Esa Rahtu, and Arno Solin. Gaussian splatting on the move: Blur and rolling shutter compensation for natural camera motion. In *European conference on computer vision*, pages 160–177, 2024. 2, 8
- [42] Christiane Sommer, Vladyslav Usenko, David Schubert, Nikolaus Demmel, and Daniel Cremers. Efficient Derivative Computation for Cumulative B-Splines on Lie Groups. In *2020 IEEE/CVF Conference on Computer Vision and Pattern Recognition (CVPR)*, pages 11145–11153, 2020. 7, 1, 2
- [43] Lukas von Stumberg and Daniel Cremers. DM-VIO: Delayed Marginalization Visual-Inertial Odometry. *IEEE Robotics and Automation Letters*, 7(2):1408–1415, 2022. 7
- [44] Lisong C Sun, Neel P Bhatt, Jonathan C Liu, Zhiwen Fan, Zhangyang Wang, Todd E Humphreys, and Ufuk Topcu. Mm3dgs slam: Multi-modal 3d gaussian splatting for slam using vision, depth, and inertial measurements. In *2024 IEEE/RSJ International Conference on Intelligent Robots and Systems (IROS)*, pages 10159–10166, 2024. 2, 3
- [45] Zachary Teed and Jia Deng. Tangent space backpropagation for 3d transformation groups. In *Proceedings of the IEEE/CVF conference on computer vision and pattern recognition*, pages 10338–10347, 2021. 7, 1, 2
- [46] Zachary Teed and Jia Deng. DROID-SLAM: Deep Visual SLAM for Monocular, Stereo, and RGB-D Cameras. In *Advances in Neural Information Processing Systems*, pages 16558–16569, 2021. 2, 7, 8
- [47] Fabio Tosi, Youmin Zhang, Ziren Gong, Erik Sandström, Stefano Mattoccia, Martin R. Oswald, and Matteo Poggi. How NeRFs and 3D Gaussian Splatting are Reshaping SLAM: a Survey, 2024. arXiv:2402.13255 [cs]. 2
- [48] Benjamin Ronald Van Manen, Victor Sluiter, and Abeje Yenehun Mersha. FirebotSLAM: Thermal SLAM to Increase Situational Awareness in Smoke-Filled Environments. *Sensors*, 23(17):7611, 2023. 1, 2
- [49] Stephen Vidas, Ruan Lakemond, Simon Denman, Clinton Fookes, Sridha Sridharan, and Tim Wark. An Exploration of Feature Detector Performance in the Thermal-Infrared Modality. In *2011 International Conference on Digital Image Computing: Techniques and Applications*, pages 217–224, 2011. 2
- [50] Chen Wang, Dasong Gao, Kuan Xu, Junyi Geng, Yaoyu Hu, Yuheng Qiu, Bowen Li, Fan Yang, Brady Moon, Abhinav Pandey, Aryan, Jiahe Xu, Tianhao Wu, Haonan He, Daning Huang, Zhongqiang Ren, Shibo Zhao, Taimeng Fu, Pranay Reddy, Xiao Lin, Wenshan Wang, Jingnan Shi, Rajat Talak, Kun Cao, Yi Du, Han Wang, Huai Yu, Shanzhao Wang, Siyu Chen, Ananth Kashyap, Rohan Bandaru, Karthik Dantu,

- Jiajun Wu, Lihua Xie, Luca Carlone, Marco Hutter, and Sebastian Scherer. PyPose: A library for robot learning with physics-based optimization. In *IEEE/CVF Conference on Computer Vision and Pattern Recognition (CVPR)*, 2023. 7, 1, 2, 3
- [51] Peng Wang, Lingzhe Zhao, Ruijie Ma, and Peidong Liu. BAD-NeRF: Bundle Adjusted Deblur Neural Radiance Fields. In *2023 IEEE/CVF Conference on Computer Vision and Pattern Recognition (CVPR)*, pages 4170–4179, 2023. 1, 2
- [52] Peng Wang, Lingzhe Zhao, Yin Zhang, Shiyu Zhao, and Peidong Liu. Mba-slam: Motion blur aware dense visual slam with radiance fields representation. *IEEE Transactions on Pattern Analysis and Machine Intelligence*, 2025. 1, 3
- [53] Yu Wang, Haoyao Chen, Yufeng Liu, and Shiwu Zhang. Edge-Based Monocular Thermal-Inertial Odometry in Visually Degraded Environments. *IEEE Robotics and Automation Letters*, 8(4):2078–2085, 2023. 1, 2
- [54] Ke Wu, Zicheng Zhang, Muer Tie, Ziqing Ai, Zhongxue Gan, and Wenchao Ding. Vings-mono: Visual-inertial gaussian splatting monocular slam in large scenes. *IEEE Transactions on Robotics*, 41:5912–5931, 2025. 3
- [55] Qi Wu, Janick Martinez Esturo, Ashkan Mirzaei, Nicolas Moenne-Loccoz, and Zan Gojic. 3dgut: Enabling distorted cameras and secondary rays in gaussian splatting. In *Proceedings of the Computer Vision and Pattern Recognition Conference*, pages 26036–26046, 2025. 2
- [56] Yuzhen Wu, Lingxue Wang, Lian Zhang, Mingkun Chen, Wenqu Zhao, Dezhi Zheng, and Yi Cai. Monocular thermal slam with neural radiance fields for 3d scene reconstruction. *Neurocomputing*, 617:129041, 2025. 1, 2, 3
- [57] P.V. Karthik Yadav, Isha Yadav, B. Ajitha, Abraham Rajasekar, Sudha Gupta, and Y. Ashok Kumar Reddy. Advancements of uncooled infrared microbolometer materials: A review. *Sensors and Actuators A: Physical*, 342:113611, 2022. 1
- [58] Vickie Ye, Ruilong Li, Justin Kerr, Matias Turkulainen, Brent Yi, Zhuoyang Pan, Otto Seiskari, Jianbo Ye, Jeffrey Hu, Matthew Tancik, et al. gsplat: An open-source library for gaussian splatting. *Journal of Machine Learning Research*, 26(34):1–17, 2025. 2, 7, 6
- [59] Zehao Yu, Anpei Chen, Binbin Huang, Torsten Sattler, and Andreas Geiger. Mip-splatting: Alias-free 3d gaussian splatting. In *Proceedings of the IEEE/CVF conference on computer vision and pattern recognition*, pages 19447–19456, 2024. 7
- [60] Lingzhe Zhao, Peng Wang, and Peidong Liu. Bad-gaussians: Bundle adjusted deblur gaussian splatting. In *European Conference on Computer Vision*, pages 233–250, 2024. 1, 2
- [61] Shibo Zhao, Peng Wang, Hengrui Zhang, Zheng Fang, and Sebastian Scherer. TP-TIO: A Robust Thermal-Inertial Odometry with Deep ThermalPoint. In *2020 IEEE/RSJ International Conference on Intelligent Robots and Systems (IROS)*, pages 4505–4512, 2020. 1, 2
- [62] Yuxuan Zhou, Xingxing Li, Shengyu Li, Xuanbin Wang, Shaoquan Feng, and Yuxuan Tan. Dba-fusion: tightly integrating deep dense visual bundle adjustment with multiple sensors for large-scale localization and mapping. *IEEE Robotics and Automation Letters*, 9(7):6138–6145, 2024. 7, 8
- [63] Liyuan Zhu, Yue Li, Erik Sandström, Shengyu Huang, Konrad Schindler, and Iro Armeni. Loopsplat: Loop closure by registering 3d gaussian splats. In *2025 International Conference on 3D Vision (3DV)*, pages 156–167, 2025. 9
- [64] Zihan Zhu, Songyou Peng, Viktor Larsson, Zhaopeng Cui, Martin R Oswald, Andreas Geiger, and Marc Pollefeys. Nicerslam: Neural implicit scene encoding for rgb slam. In *2024 International Conference on 3D Vision (3DV)*, pages 42–52, 2024. 2
- [65] Jon Zubizarreta, Iker Aguinaga, and Jose Maria Martinez Montiel. Direct sparse mapping. *IEEE Transactions on Robotics*, 36(4):1363–1370, 2020. 3, 7
- [66] David Zuñiga-Noël, Francisco-Angel Moreno, and Javier Gonzalez-Jimenez. An analytical solution to the imu initialization problem for visual-inertial systems. *IEEE Robotics and Automation Letters*, 6(3):6116–6122, 2021. 7

TRGS-SLAM: IMU-Aided Gaussian Splatting SLAM for Blurry, Rolling Shutter, and Noisy Thermal Images

Supplementary Material

In this supplementary material, we provide additional details on our B-spline implementation (Sec. A), *undistorted* microbolometer image model (Sec. B), discrete approximation of motion blur (Sec. C), mapping optimization (Sec. D), modified gradient accumulation (Sec. E), and trajectory transformations applied after IMU initialization and IMU updates (Sec. F). We also provide additional details on the dataset we run on (Sec. G) and the parameter values we use in all runs (Sec. H). Moreover, we provide supplementary results in the form of an ablation study (Sec. I) and further timing analysis (Sec. J). Finally, we provide a broader discussion of the limitations of our method (Sec. K).

A. B-Spline Implementation Details

We introduce a standalone package for B-spline optimization in PyTorch. The package supports B-splines in \mathbb{R}^d and $\text{SO}(3)$. This section describes our trajectory implementation specifically, but the expressions involving position can generalize to \mathbb{R}^d (and we exploit this to implement the FPN components with splines in \mathbb{R}^{wh} and \mathbb{R}). The functionality described in Sec. A.5 for extending the B-splines, fitting them to predictions, and making constant velocity predictions, is also included in the package (but IMU integration is implemented separately).

A.1. B-spline Formulation

As stated in Sec. 3.2, we represent the continuous-time trajectory using two separate uniform B-splines for position $\mathbf{p}(t) \in \mathbb{R}^3$ and rotation $\mathbf{R}(t) \in \text{SO}(3)$. Specifically, we use a non-cumulative B-spline for the positions, and a cumulative B-spline for the rotations. At time $t \in [t_i, t_{i+1})$, the position and rotation are given as:

$$\begin{aligned} \mathbf{p}(t) &= [\mathbf{p}_i \quad \mathbf{p}_{i+1} \quad \dots \quad \mathbf{p}_{i+k-1}] \mathbf{M}^{(k)} \mathbf{u} = \mathbf{P}_i^{(k)} \mathbf{M}^{(k)} \mathbf{u} \\ \mathbf{R}(t) &= \mathbf{R}_i \prod_{j=1}^{k-1} \text{Exp}(\lambda_j(t) \text{Log}(\mathbf{R}_{i+j-1}^{-1} \mathbf{R}_{i+j})) \\ \lambda(t) &= \mathbf{M}^{*(k)} \mathbf{u}, \mathbf{u} = [1 \quad u \quad \dots \quad u^{k-1}]^T, u = \frac{t - t_i}{\Delta t_c} \end{aligned} \quad (18)$$

where k is the order of the splines, $\{\mathbf{p}_i\}_{i=0}^{N_c-1}$ and $\{\mathbf{R}_i\}_{i=0}^{N_c-1}$ are the position and rotation control points, $\{t_i\}_{i=0}^{N_c-1}$ are the knots, $\Delta t_c = t_{i+1} - t_i \forall i$ is the knot interval, and $\mathbf{M}^{(k)}$ and $\mathbf{M}^{*(k)}$ are the non-cumulative and cumulative blending matrices, respectively. Note that for uniform B-splines (those with constant Δt_c) both $\mathbf{M}^{(k)}$ and $\mathbf{M}^{*(k)}$ are constant and determined solely by the spline order k [42].

A.2. B-spline Derivatives

Given the definitions of the position and rotation splines in Eq. (18), the linear velocity $\mathbf{v}(t)$ and acceleration $\mathbf{a}(t)$ can be computed as:

$$\begin{aligned} \mathbf{v}(t) &= \mathbf{P}_i^{(k)} \mathbf{M}^{(k)} \dot{\mathbf{u}}, \quad \mathbf{a}(t) = \mathbf{P}_i^{(k)} \mathbf{M}^{(k)} \ddot{\mathbf{u}} \\ \dot{\mathbf{u}} &= \frac{1}{\Delta t_c} [0 \quad 1 \quad 2u \quad \dots \quad (k-1)u^{k-2}]^T \\ \ddot{\mathbf{u}} &= \frac{1}{\Delta t_c^2} [0 \quad 0 \quad 2 \quad 6u \quad \dots \quad (k-1)(k-2)u^{k-3}]^T \end{aligned} \quad (19)$$

and we can compute the angular velocity $\boldsymbol{\omega}(t)$ directly by applying the following efficient recursive expression from $j = 1$ to $j = k$ [42]:

$$\begin{aligned} \boldsymbol{\omega}^{(j)}(t) &= (\mathbf{A}_{j-1}^i(t))^{-1} \boldsymbol{\omega}^{(j-1)}(t) + \dot{\lambda}_{j-1}(t) \mathbf{d}_{j-1}^i \\ \mathbf{A}_j^i(t) &= \text{Exp}(\lambda_j(t) \mathbf{d}_j^i), \quad \mathbf{d}_j^i = \text{Log}(\mathbf{R}_{i+j-1}^{-1} \mathbf{R}_{i+j}) \\ \dot{\lambda}(t) &= \mathbf{M}^{*(k)} \dot{\mathbf{u}}, \quad \boldsymbol{\omega}^{(1)}(t) = \mathbf{0} \end{aligned} \quad (20)$$

A.3. On-Manifold Parameter Updates, Efficient Forward Passes, & Analytical Backward Passes for $\text{SO}(3)$ B-Splines

One common approach to optimizing rotations in PyTorch is to store them in the minimal axis-angle format, apply the exponential and logarithm maps to convert to and from rotation matrices as needed, and rely on PyTorch’s default tools for automatic differentiation and optimization. Storing the parameters as axis-angle vectors ensures they remain valid rotations, but the standard PyTorch backward passes through the exponential and logarithm maps include numerically unstable terms [45]. It is more stable and accurate to compute tangent space gradients through custom backward passes and perform on-manifold parameter updates [45]. PyPose [50] and LieTorch [45] are PyTorch libraries that provide this functionality.

In our package, we implement the rotation spline to return a `pypose.SO3` [50] or `lietorch.SO3` [45] object when it is evaluated (Eq. (18)). In either case, this ensures that the gradients for the returned rotations are computed in the tangent space. Our custom backward passes, described below, also compute gradients in the tangent space, and we perform on-manifold updates to the rotation control points in optimization. That is, an update step for control point \mathbf{R}_i is performed as $\mathbf{R}_i \leftarrow \text{Exp}(\boldsymbol{\delta}_i) \mathbf{R}_i$ where $\boldsymbol{\delta}_i$ is the optimizer increment computed from the tangent space gradient of \mathbf{R}_i .

We implement three different versions of the forward

Table 3. Timing comparison between different versions of our rotation spline.

Version	Device	Number of Timestamps Evaluated	Rotation Loss Compute Time (ms)		Ang. Vel. Loss Compute Time (ms)	
			Forward	Backward	Forward	Backward
			PyPose	CPU	1k	5.45
LieTorch	CPU	1k	1.68	1.39	1.82	1.48
C++	CPU	1k	0.59	0.41	0.51	0.27
PyPose	GPU	1k	14.30	13.74	15.44	15.55
LieTorch	GPU	1k	3.11	2.12	4.28	2.28
C++	GPU	1k	0.81	0.38	0.73	0.30
PyPose	CPU	100k	34.70	89.19	30.76	91.55
LieTorch	CPU	100k	44.99	80.67	43.78	85.54
C++	CPU	100k	16.65	14.47	11.16	3.20
PyPose	GPU	100k	14.87	15.63	15.25	17.43
LieTorch	GPU	100k	3.93	2.37	4.20	2.38
C++	GPU	100k	18.90	1.22	33.89	1.11

passes for evaluating the rotation spline Eq. (18) and its angular velocity Eq. (20): one using PyPose [50], one using LieTorch [45], and one using multi-threaded C++ functions that run on the CPU and are called through Python bindings. We leave the backward passes for the LieTorch and PyPose versions to be handled automatically by their respective libraries. For the C++ version, we implement custom backward passes utilizing the efficient algorithms given in [42] for computing the Jacobians of the rotations and angular velocities with respect to the control points. To avoid redundant calculations, these Jacobians are computed in the forward pass and stored for the backward pass if gradients are needed.

Table 3 shows a timing comparison between the three versions we implemented, operating with a NVIDIA RTX A6000 GPU and an AMD Ryzen 9 5950X CPU. The comparison shows the time taken for the forward and backward pass of computing a rotation loss (similar to Eq. (23)) and an angular velocity loss (similar to Eq. (7), without the accelerometer term). The table shows results for the splines being evaluated at 1k timestamps and 100k timestamps, with the control points stored on the CPU or GPU. Note that when our C++ implementation is used with the control points stored on the GPU, data is transferred to the CPU for the forward pass only. The results indicate that the C++ version, with control points stored on the CPU, is the most efficient when the spline is evaluated at a relatively small number of timestamps, while the LieTorch version, with control points stored on the GPU, is the fastest with a large number of timestamps. Therefore, we use the C++ version in SLAM, with the trajectory control points and the IMU bias parameters stored on the CPU, and the LieTorch version in offline refinement, with all parameters stored on the GPU.

Additionally, as we generally observed LieTorch operations and backward passes to be more efficient than PyPose, we configure the rotation spline to return a `lietorch.SO3` object when evaluated in SLAM and offline refinement (regardless of whether the actual spline evaluation was per-

formed with LieTorch or our C++ implementation).

A.4. Sparse Gradients and Optimization

For each spline, we store the entire set of control points as an individual PyTorch `Parameter`. To ensure that only active control points are updated at each iteration, our spline implementations return sparse gradients and we use PyTorch’s `SparseAdam` optimizer to update them. If we were to return dense gradients and use the standard `Adam` optimizer, the inactive control point gradients would be zero, the corresponding moments in the optimizer state would be falsely updated using these zero-valued gradients, and the inactive control points themselves would be falsely updated (if their moments are non-zero from past active iterations), despite taking no part in the current loss calculation. `SparseAdam`, by contrast, only updates the moments and parameters indexed by the sparse gradient it receives. In our implementation, this is essentially equivalent to, though much more efficient than, storing the control points as individual PyTorch `Parameters` and updating them with separate `Adam` optimizers².

A.5. B-Spline Extension Details

Duplication & Fitting to Predictions As explained in Sec. 3.5, the position and rotation splines can only be evaluated for $t \in [t_0, t_0 + (N_c - k + 1)\Delta t_c]$ and control points must be added when a new image arrives. The number of new control points needed to accommodate image l is:

$$N_{\text{new}} = \lfloor \frac{t_{\text{max},l} - t_0}{\Delta t_c} \rfloor + k - N_c \quad (21)$$

These new control points are initialized by duplicating \mathbf{p}_{N_c-1} and \mathbf{R}_{N_c-1} .

After a set number of keyframes, we additionally compute N_q predicted poses at times $\{t_{\text{pred},q}\}_{q=0}^{N_q-1}$ evenly spaced over $[t'_{0,0,l-1}, t_{\text{max},l}]$ and fit the active sets of position and rotation control points,

$$\begin{aligned} \mathcal{P} &= \{\mathbf{p}_i\}_{i=\lfloor (t'_{0,0,l-1} - t_0)/\Delta t_c \rfloor}^{N_c + N_{\text{new}} - 1} \\ \mathcal{R} &= \{\mathbf{R}_i\}_{i=\lfloor (t'_{0,0,l-1} - t_0)/\Delta t_c \rfloor}^{N_c + N_{\text{new}} - 1} \end{aligned} \quad (22)$$

to these predictions. Specifically, we separately solve the following optimization problems:

$$\begin{aligned} \arg \min_{\mathcal{P}} \sum_{q=0}^{N_q-1} \|\mathbf{p}(t_{\text{pred},q}) - \mathbf{p}_{\text{pred},q}\|_2^2 \\ \arg \min_{\mathcal{R}} \sum_{q=0}^{N_q-1} \left\| \text{Log} \left((\mathbf{R}(t_{\text{pred},q}))^{-1} \mathbf{R}_{\text{pred},q} \right) \right\|_2^2 \end{aligned} \quad (23)$$

²The current PyTorch implementation of `SparseAdam` uses a single step counter to compute the bias correction. This quickly reduces to `Adam` without bias correction for new control points. We tested a custom implementation with an element-wise step counter but found empirically that this harmed performance.

where $\{\mathbf{p}_{\text{pred},q}\}_{q=0}^{N_q-1}$ and $\{\mathbf{R}_{\text{pred},q}\}_{q=0}^{N_q-1}$ are the predicted positions and rotations. N_q is set larger than the number of active control points ($N_q > N_c + N_{\text{new}} - \lfloor (t'_{0,0,l-1} - t_0)/\Delta t_c \rfloor$) to ensure the problems are overdetermined. We use the PyPose [50] implementation of Levenberg–Marquard to solve these problems within the PyTorch framework.

Note that it is necessary to fit the control points to the predictions because B-spline control points do not generally sit on the spline itself and therefore the value of the spline cannot be trivially set directly.

Constant Velocity Predictions Prior to IMU initialization, the predictions are made assuming constant velocity. The instantaneous velocities of the splines (Eqs. 19 and 20) can be noisy, especially prior to IMU initialization. Therefore, we compute finite difference estimates of the linear and angular velocities as follows:

$$\begin{aligned} \bar{\mathbf{v}}_{\text{C,avg}}^{\text{W}}(t'_{0,0,l-1}) &= \frac{\bar{\mathbf{P}}_{\text{C}}^{\text{W}}(t'_{0,0,l-1}) - \bar{\mathbf{P}}_{\text{C}}^{\text{W}}(t'_{0,0,l-1} - T_I)}{T_I} \\ \omega_{\text{C,avg}}^{\text{C}}(t'_{0,0,l-1}) &= \frac{\text{Log} \left(\left(\mathbf{R}_{\text{C}}^{\text{W}}(t'_{0,0,l-1} - T_I) \right)^{-1} \mathbf{R}_{\text{C}}^{\text{W}}(t'_{0,0,l-1}) \right)}{T_I} \end{aligned} \quad (24)$$

where T_I is the average frame period. The predicted position and rotation at time $t_{\text{pred},q}$ are then computed as:

$$\begin{aligned} \bar{\mathbf{P}}_{\text{C,pred},q}^{\text{W}} &= \bar{\mathbf{P}}_{\text{C}}^{\text{W}}(t'_{0,0,l-1}) + (t_{\text{pred},q} - t'_{0,0,l-1}) \bar{\mathbf{v}}_{\text{C,avg}}^{\text{W}}(t'_{0,0,l-1}) \\ \mathbf{R}_{\text{C,pred},q}^{\text{W}} &= \mathbf{R}_{\text{C}}^{\text{W}}(t'_{0,0,l-1}) \text{Exp} \left((t_{\text{pred},q} - t'_{0,0,l-1}) \omega_{\text{C,avg}}^{\text{C}}(t'_{0,0,l-1}) \right) \end{aligned} \quad (25)$$

IMU Integration Based Predictions After IMU initialization, the predictions are made through IMU integration. Let b denote the index of an IMU measurement taken exactly at $t'_{0,0,l-1}$ and f denote the index of the last IMU measurement taken before the prediction time $t_{\text{pred},q}$. Note that $\tilde{\omega}_{1,b}^{\text{I}}$ and $\tilde{\mathbf{a}}_{1,b}^{\text{I}}$ are interpolated using the IMU measurements taken immediately before and after $t'_{0,0,l-1}$. We compute the position and rotation at the time of the final IMU measurement $t_{\text{IMU},f}$ by integrating the IMU measurements from $t_{\text{IMU},b}$ to $t_{\text{IMU},f}$

as follows:

$$\begin{aligned} \mathbf{R}_{\text{I,IMU},f}^{\text{W}} &= \mathbf{R}_{\text{I}}^{\text{W}}(t'_{0,0,l-1}) \prod_{m=b}^{f-1} \text{Exp} \left((\tilde{\omega}_{1,m}^{\text{I}} - \mathbf{b}_{\mathbf{g}}) \Delta t_m \right) \\ \mathbf{v}_{\text{I,IMU},f}^{\text{W}} &= \mathbf{v}_{\text{I}}^{\text{W}}(t'_{0,0,l-1}) + \sum_{m=b}^{f-1} G \hat{\mathbf{g}}^{\text{W}} \Delta t_m \\ &\quad + \sum_{m=b}^{f-1} \mathbf{R}_{\text{I,IMU},m}^{\text{W}} (\tilde{\mathbf{a}}_{1,m}^{\text{I}} - \mathbf{b}_a) \Delta t_m \\ \mathbf{P}_{\text{I,IMU},f}^{\text{W}} &= \mathbf{P}_{\text{I}}^{\text{W}}(t'_{0,0,l-1}) + \sum_{m=b}^{f-1} \mathbf{v}_{\text{I,IMU},m}^{\text{W}} \Delta t_m \\ &\quad + \sum_{m=b}^{f-1} \frac{1}{2} G \hat{\mathbf{g}}^{\text{W}} \Delta t_m^2 \\ &\quad + \sum_{m=b}^{f-1} \frac{1}{2} \mathbf{R}_{\text{I,IMU},m}^{\text{W}} (\tilde{\mathbf{a}}_{1,m}^{\text{I}} - \mathbf{b}_a) \Delta t_m^2 \end{aligned} \quad (26)$$

where $\Delta t_m = t_{\text{IMU},m+1} - t_{\text{IMU},m}$. Note that in this case we do use the instantaneous linear velocity $\mathbf{v}_{\text{I}}^{\text{W}}(t'_{0,0,l-1})$ (Eq. (19)), rather than a finite difference estimate. The predicted position and rotation at time $t_{\text{pred},q}$ are then computed as:

$$\begin{aligned} \mathbf{P}_{\text{I,pred},q}^{\text{W}} &= \mathbf{P}_{\text{I,IMU},f}^{\text{W}} + \mathbf{v}_{\text{I,IMU},f}^{\text{W}} \Delta t_f + \frac{1}{2} G \hat{\mathbf{g}}^{\text{W}} \Delta t_f^2 \\ &\quad + \frac{1}{2} \mathbf{R}_{\text{I,IMU},f}^{\text{W}} (\tilde{\mathbf{a}}_{1,f}^{\text{I}} - \mathbf{b}_a) \Delta t_f^2 \\ \mathbf{R}_{\text{I,pred},q}^{\text{W}} &= \mathbf{R}_{\text{I,IMU},f}^{\text{W}} \text{Exp} \left(\tilde{\omega}_{1,f}^{\text{I}} \Delta t_f \right) \end{aligned} \quad (27)$$

where $\Delta t_f = t_{\text{pred},q} - t_{\text{IMU},f}$.

Optimizer State Management When the B-splines are extended, the control point parameters are re-initialized as the existing control points concatenated with the new ones. The optimizer states corresponding to the new control points are set to zero while the states corresponding to the existing control points are retained. Note that in the fitting process (Eq. (23)) the active sets of control points, \mathcal{P} and \mathcal{R} , include existing control points that have already been optimized through tracking and mapping. We initially restricted the B-spline extension process to only fit the N_{new} control points to the pose predictions, to avoid manipulating control points that may have already been well optimized. However, this seemingly overfit the new control points, leading to a poor initialization for tracking. It is also unclear whether the optimizer states corresponding to these modified control points should be zeroed. In practice, we have found it best to leave these optimizer states unchanged.

B. Undistorted Microbolometer Image Model

The undistortion of $\tilde{\mathbf{N}}'_l$ can be written as follows:

$$\begin{aligned} [\tilde{\mathbf{N}}'_l]_{y_p, x_p} &= \text{undistort}(\tilde{\mathbf{N}}'_l, x_p, y_p) \\ &= f_{\text{interp}}(\tilde{\mathbf{N}}'_l, \text{map}_x(x_p, y_p), \text{map}_y(x_p, y_p)) \end{aligned} \quad (28)$$

where $\text{map}_x(x_p, y_p)$ and $\text{map}_y(x_p, y_p)$ map pixel coordinates (x_p, y_p) in the undistorted image $\tilde{\mathbf{N}}'_l$ to fractional pixel coordinates in $\tilde{\mathbf{N}}'_l$, and f_{interp} denotes bilinear interpolation. $\text{map}_x(x_p, y_p)$ and $\text{map}_y(x_p, y_p)$ are precomputed from the original camera intrinsic matrix, distortion parameters, and the new camera matrix. Bilinear interpolation is used here to estimate the value of $\tilde{\mathbf{N}}'_l$ at the fractional pixel coordinates and it can be written as:

$$f_{\text{interp}}(\mathbf{Q}, x, y) = \sum_{i \in \{0,1\}} \sum_{j \in \{0,1\}} w_{ij}[\mathbf{Q}]_{y_f+j, x_f+i} \quad (29)$$

where $x_f = \lfloor x \rfloor$, $y_f = \lfloor y \rfloor$, and $\{w_{00}, w_{01}, w_{10}, w_{11}\}$ are weights computed based the relative proximity of (x, y) to the four neighboring integer coordinates. Note that these weights sum to 1.

Let $x = \text{map}_x(x_p, y_p)$ and $y = \text{map}_y(x_p, y_p)$. We can then write:

$$\begin{aligned} [\tilde{\mathbf{N}}_l]_{y_p, x_p} &= \\ &= \sum_{i \in \{0,1\}} \sum_{j \in \{0,1\}} w_{ij} \tilde{n}'_{x_f+i, y_f+j}(t'_{x_f+i, y_f+j, l}) \end{aligned} \quad (30)$$

Given that the four neighboring pixels span only two rows, their readout times differ only slightly. Therefore, we define the effective readout time of the pixel (x_p, y_p) in the undistorted image as:

$$t_{x_p, y_p, l} = \sum_{i \in \{0,1\}} \sum_{j \in \{0,1\}} w_{ij} t'_{x_f+i, y_f+j, l} \quad (31)$$

With this effective readout time, we can then write $[\tilde{\mathbf{N}}_l]_{y_p, x_p} = \tilde{n}_{x_p, y_p}(t_{x_p, y_p, l})$ and approximate Eq. (30) as:

$$[\tilde{\mathbf{N}}_l]_{y_p, x_p} \approx \sum_{i \in \{0,1\}} \sum_{j \in \{0,1\}} w_{ij} \tilde{n}'_{x_f+i, y_f+j}(t_{x_p, y_p, l}) \quad (32)$$

Next, by expanding $\tilde{n}'_{x_f+i, y_f+j}(t_{x_p, y_p, l})$ and distributing the sum, we can write $\tilde{n}_{x_p, y_p}(t_{x_p, y_p, l})$ in the form of Eqs. 1 and 2:

$$\tilde{n}_{x_p, y_p}(t_{x_p, y_p, l}) = \tilde{m}_{x_p, y_p}(t_{x_p, y_p, l}) + \tilde{o}_{x_p, y_p}(t_{x_p, y_p, l}) \quad (33)$$

$$\begin{aligned} \tilde{m}_{x_p, y_p}(t_{x_p, y_p, l}) &= \\ &= \frac{1}{\tau} \int_{-\infty}^{t_{x_p, y_p, l}} \exp\left(\frac{s - t_{x_p, y_p, l}}{\tau}\right) \tilde{p}_{x_p, y_p}(s) ds \end{aligned} \quad (34)$$

where $\tilde{m}_{x_p, y_p}(t)$, $\tilde{o}_{x_p, y_p}(t)$ and $\tilde{p}_{x_p, y_p}(t)$ are defined as:

$$\tilde{m}_{x_p, y_p}(t) = \sum_{i \in \{0,1\}} \sum_{j \in \{0,1\}} w_{ij} \tilde{m}'_{x_f+i, y_f+j}(t) \quad (35)$$

$$\tilde{o}_{x_p, y_p}(t) = \sum_{i \in \{0,1\}} \sum_{j \in \{0,1\}} w_{ij} \tilde{o}'_{x_f+i, y_f+j}(t) \quad (36)$$

$$\tilde{p}_{x_p, y_p}(t) = \sum_{i \in \{0,1\}} \sum_{j \in \{0,1\}} w_{ij} \tilde{p}'_{x_f+i, y_f+j}(t) \quad (37)$$

In summary, the undistorted image can be written as $[\tilde{\mathbf{N}}_l]_{y_p, x_p} = \tilde{n}_{x_p, y_p}(t_{x_p, y_p, l})$ where the individual pixel values $\tilde{n}_{x_p, y_p}(t_{x_p, y_p, l})$ can be written in the same form as Eqs. 1 and 2, but the readout time is determined by Eq. (31).

Note that the effective readout time in Eq. (31) can be easily computed using the same undistortion operation applied to the images. Let $\mathbf{T}'_{\text{roll}}$ be a lookup table of the readout times in the distorted image, relative to $t'_{0,0,l}$. That is, $[\mathbf{T}'_{\text{roll}}]_{y_p, x_p} = x_p \Delta t_{\text{pix}} + y_p w \Delta t_{\text{pix}}$. If we expand Eq. (31):

$$\begin{aligned} t_{x_p, y_p, l} &= \sum_{i \in \{0,1\}} \sum_{j \in \{0,1\}} w_{ij} t'_{0,0,l} \\ &+ \sum_{i \in \{0,1\}} \sum_{j \in \{0,1\}} w_{ij} [\mathbf{T}'_{\text{roll}}]_{y_f+j, x_f+i} \\ &= t'_{0,0,l} + \sum_{i \in \{0,1\}} \sum_{j \in \{0,1\}} w_{ij} [\mathbf{T}'_{\text{roll}}]_{y_f+j, x_f+i} \end{aligned} \quad (38)$$

it becomes clear from comparison to Eqs. 28 and 29 that this can be written as:

$$\begin{aligned} t_{x_p, y_p, l} &= t'_{0,0,l} + \text{undistort}(\mathbf{T}'_{\text{roll}}, x_p, y_p) \\ &= t'_{0,0,l} + [\mathbf{T}_{\text{roll}}]_{y_p, x_p} \end{aligned} \quad (39)$$

Finally, note that we also downsample the images prior to undistortion. We downsample by block averaging, using a block size the image dimensions are divisible by. Following a process similar to the preceding discussion on undistortion, it can be shown that this block averaging approximately preserves the image formation model but with new effective readout times. In this case, the new readout times follow the original expression given in Eq. (3), but with Δt_{pix} multiplied by the square of the block size.

C. Discrete Approximation of Motion Blur

As explained in Sec. 3.3, to compute $[\mathbf{M}_l]_{y_p, x_p} = m_{x_p, y_p}(t_{x_p, y_p, l})$ we rasterize N_r images at times $\{t_r\}_{r=0}^{N_r-1}$ evenly spaced over $[t_{\text{max}, l} - T_b, t_{\text{max}, l}]$ where $t_{\text{max}, l}$ is defined as:

$$t_{\text{max}, l} = t'_{0,0,l} + \max(\mathbf{T}_{\text{roll}}) \quad (40)$$

Focusing on a single pixel, this means we have N_r samples $\{p_{x_p, y_p}(t_r)\}_{r=0}^{N_r-1}$ and need to compute an estimate of the blurry pixel value $m_{x_p, y_p}(t_{x_p, y_p, l})$ with a discrete approximation of Eq. (34). In the following derivation we

assume the most general case: the effective readout time falls between two samples, i.e., $t_n < t_{x_p, y_p, l} < t_{n+1}$ for some n where $0 \leq n < N_r - 1$.

To compute $m_{x_p, y_p}(t_{x_p, y_p, l})$ we treat $p_{x_p, y_p}(t_r)$ as linear between samples, and break Eq. (34) up into a sum of integrals over consecutive samples. Let t_a and t_b be consecutive sample times with $t_b \leq t_n$. Dropping the pixel coordinate subscripts for readability, we can write the portion of the integral in Eq. (34) from t_a to t_b as:

$$\begin{aligned} & \frac{1}{\tau} \int_{t_a}^{t_b} \exp\left(\frac{s-t_l}{\tau}\right) p(s) ds = \\ & \frac{1}{\tau} \int_{t_a}^{t_b} \exp\left(\frac{s-t_l}{\tau}\right) (p(t_a) + v_{a,b}(s-t_a)) ds \end{aligned} \quad (41)$$

where $v_{a,b}$ is the slope of $p(t)$ between t_a and t_b :

$$\begin{aligned} v_{a,b} &= \frac{p(t_b) - p(t_a)}{t_b - t_a} = \frac{p(t_b) - p(t_a)}{\Delta t_r}, \\ \Delta t_r &= \frac{T_b}{N_r - 1} \end{aligned} \quad (42)$$

The result of Eq. (41) is:

$$\begin{aligned} & \left[\exp\left(\frac{s-t_l}{\tau}\right) (p(t_a) - v_{a,b}(t_a - s + \tau)) \right]_{t_a}^{t_b} = \\ & \left[\exp\left(\frac{s-t_l}{\tau}\right) ((p(t_a) + v_{a,b}(s-t_a)) - v_{a,b}\tau) \right]_{t_a}^{t_b} = \\ & \left[\exp\left(\frac{s-t_l}{\tau}\right) (p(s) - v_{a,b}\tau) \right]_{t_a}^{t_b} \end{aligned} \quad (43)$$

Evaluating Eq. (43), substituting in Eq. (42), letting $E_a = \exp\left(\frac{t_a-t_l}{\tau}\right)$ and $E_b = \exp\left(\frac{t_b-t_l}{\tau}\right)$, and grouping terms by $p(t_a)$ and $p(t_b)$ we get:

$$\begin{aligned} & \frac{1}{\tau} \int_{t_a}^{t_b} \exp\left(\frac{s-t_l}{\tau}\right) p(s) ds = \\ & p(t_a) \left(E_b \frac{\tau}{\Delta t_r} - E_a \left(1 + \frac{\tau}{\Delta t_r}\right) \right) \\ & + p(t_b) \left(E_b \left(1 - \frac{\tau}{\Delta t_r}\right) + E_a \frac{\tau}{\Delta t_r} \right) \end{aligned} \quad (44)$$

Next, because $t_n < t_l < t_{n+1}$, the portion of the integral in Eq. (34) from t_n to t_l is computed as:

$$\begin{aligned} & \frac{1}{\tau} \int_{t_n}^{t_l} \exp\left(\frac{s-t_l}{\tau}\right) p(s) ds = \\ & \left[\exp\left(\frac{s-t_l}{\tau}\right) (p(s) - v_{n,n+1}\tau) \right]_{t_n}^{t_l} = \\ & p(t_n) \left(1 - \frac{t_l - t_n}{\Delta t_r} + \frac{\tau}{\Delta t_r} - E_n \left(1 + \frac{\tau}{\Delta t_r}\right) \right) \\ & + p(t_{n+1}) \left(\frac{t_l - t_n}{\Delta t_r} - \frac{\tau}{\Delta t_r} + E_n \frac{\tau}{\Delta t_r} \right) \end{aligned} \quad (45)$$

Putting this together we can write:

$$\frac{1}{\tau} \int_{t_{\max, l} - T_b}^{t_l} \exp\left(\frac{s-t_l}{\tau}\right) p(s) ds = \sum_{r=0}^{N_r-1} (h_r + d_r) p(t_r) \quad (46)$$

where h_r and d_r are set based on the grouped terms in Eqs. 44 and 45, respectively. Specifically, using $j = \lfloor \frac{t_l - t_r}{\Delta t_r} \rfloor$, h_r and d_r are defined as:

$$h_r = \begin{cases} 0 & \text{if } j < 0 \\ 0 & \text{if } j = 0, r = 0 \\ E_r \left(1 - \frac{\tau}{\Delta t_r}\right) + E_{r-1} \frac{\tau}{\Delta t_r} & \text{if } j = 0, r \neq 0 \\ E_{r+1} \frac{\tau}{\Delta t_r} - E_r \left(1 + \frac{\tau}{\Delta t_r}\right) & \text{if } j > 0, r = 0 \\ \frac{\tau}{\Delta t_r} (E_{r-1} - 2E_r + E_{r+1}) & \text{if } j > 0, r \neq 0 \end{cases} \quad (47)$$

$$d_r = \begin{cases} \frac{t_l - t_{r-1}}{\Delta t_r} - \frac{\tau}{\Delta t_r} + E_{r-1} \frac{\tau}{\Delta t_r} & \text{if } j = -1 \\ 1 - \frac{t_l - t_r}{\Delta t_r} + \frac{\tau}{\Delta t_r} - E_r \left(1 + \frac{\tau}{\Delta t_r}\right) & \text{if } j = 0 \\ 0 & \text{else} \end{cases} \quad (48)$$

Note that the cases involving j are used to determine whether the sample $p(t_r)$ contributes to a full segment (Eq. (44)), partial segment (Eq. (45)), or both. For $r \neq 0$:

- $j = -1$ implies r is the right endpoint of the partial segment ($r = n + 1$ in Eq. (45)), only
- $j = 0$ implies r is the left endpoint of the partial segment ($r = n$ in Eq. (45)) and the right endpoint of the last full segment ($r = b$ in Eq. (44))
- $j > 0$ implies r is an interior point, acting as both the left endpoint and right endpoint of two consecutive full segments ($r = a$ and $r = b$ in Eq. (44))

In the special case of the first sample, $r = 0$:

- $j = 0$ implies r is the left endpoint of the partial segment ($r = n$ in Eq. (45)), only
- $j > 0$ implies r is the left endpoint of a full segment ($r = a$ in Eq. (44)), only

Given that the integral in Eq. (34) is unbounded, the result of the truncated integral in Eq. (46) may be significantly smaller than the true value. To approximately compensate for this we consider the case of constant $p(t) = p$. In this case, the result of the unbounded integral in Eq. (34) is p and the result of Eq. (46) is:

$$\begin{aligned} & \frac{p}{\tau} \int_{t_{\max, l} - T_b}^{t_l} \exp\left(\frac{s-t_l}{\tau}\right) ds = \\ & p \left(1 - \exp\left(\frac{t_{\max, l} - T_b - t_l}{\tau}\right) \right) \end{aligned} \quad (49)$$

Therefore, we compute the pixel-wise correction factor as:

$$g = \left(1 - \exp\left(\frac{t_{\max, l} - T_b - t_l}{\tau}\right) \right)^{-1} \quad (50)$$

The final expression for $m_{x_p, y_p}(t_{x_p, y_p, l})$ is:

$$m_{x_p, y_p}(t_{x_p, y_p, l}) = g_{x_p, y_p} \sum_{r=0}^{N_r-1} (h_{x_p, y_p, r} + d_{x_p, y_p, r}) p_{x_p, y_p}(t_r) \quad (51)$$

where the pixel coordinate subscripts have been reintroduced for clarity.

Finally, we can construct the weight matrix \mathbf{W}_r as:

$$[\mathbf{W}_r]_{y_p, x_p} = g_{x_p, y_p} (h_{x_p, y_p, r} + d_{x_p, y_p, r}) \quad (52)$$

Pivotaly, $[\mathbf{W}_r]_{y_p, x_p}$ is not dependent on the absolute read-out time of the pixel $t_{x_p, y_p, l}$. Rather, $[\mathbf{W}_r]_{y_p, x_p}$ is only dependent on the relative time offsets between $t_{x_p, y_p, l}$ and the raster times $\{t_r\}_{r=0}^{N_r-1}$. Therefore, the weight matrices $\{\mathbf{W}_r\}_{r=0}^{N_r-1}$ can be precomputed.

D. Mapping Optimization Details

In Sec. 3.6 it was mentioned that \mathcal{W}_I and \mathcal{S}_I are disjoint sets of IMU measurements associated with \mathcal{W}_K and \mathcal{S}_K . Specifically, the full set of IMU measurements used in a given mapping iteration \mathcal{I}_{map} is the union of all sets of IMU measurements taken over $[\min(t_{0,0,p}, t_{\max,l} - T_b), t_{\max,l}]$ for each keyframe image l , where p denotes the image index of the keyframe prior to l . The measurements are split into \mathcal{W}_I or \mathcal{S}_I depending on whether they came after or before $t_{\max,l}$ of the latest randomly sampled keyframe, respectively.

The weighting applied in the mapping loss (Eq. (16)) is intended to prevent the existing map from being overwritten when it is re-observed from an incorrect pose. In this instance, we want any well-constrained portions of the map to remain largely unchanged and we want the error in the current keyframe window pose estimates to be corrected. Applying the weighting in Eq. (16) with $\lambda_s > \lambda_w$ reduces the relative impact of the keyframe window views on the Gaussians, but it also has a few unintended consequences. First, the weighting reduces the gradients of the position and rotation control points that contribute to the keyframe window views. Reducing these gradients runs counter to the goal of correcting the keyframe window pose error, so we manually divide these gradients by λ_w/F , where F is a set value (10 in all experiments). Second, the weighting similarly increases the gradients of the position and rotation control points that contribute to the randomly sampled keyframe views. We want these views to remain stable so we correct this by manually dividing these gradients by λ_s . Third, it has undesirable effects on the gradients of the Gaussians that are viewed primarily by the keyframe window or randomly sampled keyframes. For example, if the sets of Gaussians viewed by the keyframe window and the randomly sampled keyframes are disjoint, then the Gaussians

viewed by the keyframe window will be updated too gradually, while the Gaussians seen by the randomly sampled keyframes will be updated too aggressively. We account for this by manually reweighting the gradient of each Gaussian parameter based on the fraction of the keyframes it appears in being randomly sampled versus in the keyframe window. Specifically, we divide a Gaussian's gradients by $\lambda_s(N_S/N_W) + \lambda_w(1 - N_S/N_W)$ where N_S is the number of randomly sampled keyframes that view the Gaussian and N_W is the number of keyframes in the window that view the Gaussian.

Finally, note that we blend a random background intensity with each raster $\mathbf{I}_G(t_r)$ during mapping optimization (but not during tracking). This is done to encourage high opacities.

E. Modified Gradient Accumulation

In gsplat [58], the image plane gradients of each Gaussian are normalized such that a single image plane gradient threshold can be consistently applied, regardless of the image resolution or the batch size of renders used per iteration. The mean of the normalized image plane gradients is computed over multiple iterations by summing them and maintaining a count of the number of rasters each Gaussian was visible in. When it comes time to apply the threshold, the mean is computed by dividing the sum by the count. Our microbolometer-aware rendering scheme complicates this because we compute multiple rasters per render and the rasters are weighted differently. To account for this, we similarly normalize the image plane gradients, but we compute the "count" differently. Instead of incrementing the count by 1 for each raster the Gaussian is visible in, we increment the count using the value of the weight matrix \mathbf{W}_r associated with that raster, evaluated at the Gaussian's projected 2D image coordinate.

F. IMU Initialization & Update Details

When the IMU is initialized, the trajectory is transformed into the IMU frame with absolute scale by directly transforming the position \mathbf{p}_i and rotation \mathbf{R}_i control points as follows:

$$\begin{aligned} \mathbf{p}_i &\leftarrow \mathbf{R}_i \mathbf{p}_I^C + S \mathbf{p}_i \\ \mathbf{R}_i &\leftarrow \mathbf{R}_i \mathbf{R}_I^C \end{aligned} \quad (53)$$

where S is the estimated scale factor and \mathbf{p}_I^C and \mathbf{R}_I^C are the inverted IMU extrinsics $\mathbf{T}_C^I(t) = [\mathbf{R}_I^C, \mathbf{p}_I^C]$.

When the IMU parameters are updated, the scale update is applied by directly transforming the position control points as follows:

$$\begin{aligned} \mathbf{p}_i &\leftarrow (\mathbf{R}_i \mathbf{p}_I^C + \mathbf{p}_i) / S_{\text{prev}} \\ \mathbf{p}_i &\leftarrow \mathbf{R}_i \mathbf{R}_C^I \mathbf{p}_I^C + S_{\text{new}} \mathbf{p}_i \end{aligned} \quad (54)$$

where S_{prev} is the previous scale estimate and S_{new} is the new scale estimate.

Note that applying a rotation to the rotation control points, as in Eq. (53), exactly rotates the entire spline, but the transformations made to the position control points do not exactly apply these transformations to the position spline itself. However, we have found this error to be negligible in practice. Also note that after we apply these transformations we reinitialize the trajectory and IMU bias optimizers with zeroed states.

G. Dataset Details

The TRNeRF dataset [7] was collected with two 640×512 60 Hz thermal cameras (FLIR ADK), and a 400 Hz IMU (VectorNav VN-100). The thermal time constant of the FLIR ADK cameras is $\tau = 8$ ms and the readout time per pixel is $\Delta t_{\text{pix}} = 0.043 \mu\text{s}$. To assess the impact of onboard noise filters, only one camera had them enabled. Unless otherwise noted, we run on the unfiltered data. We process a superset of the data tested on in TRNeRF, including 10 second, medium-speed segments at the start of each sequence that aid IMU initialization. Specifically, we run on 230, 160, and 100 seconds of data in the slow, medium, and fast sequences respectively. We obtain pseudo ground truth poses through stereo visual structure from motion, as outlined in TRNeRF, replacing COLMAP [40] with GLOMAP [35] and using it on 4k images per scene prior to hloc [39]. To evaluate restoration/rendering quality, the dataset provides pseudo ground truth images for each medium and fast sequence.

Note that the TRNeRF dataset [7] is one of few thermal SLAM datasets that offer the types of aggressive camera motion we target with our method. Moreover, as highlighted in our ablation study (Sec. I), it seems that onboard noise filters can significantly violate the precise camera modeling our method relies on³. These filters are enabled by default, making it likely (but unclear) that they are enabled in datasets where this setting was not mentioned. Similarly, many thermal cameras have an optional Automatic Gain Control (AGC) feature that returns 8-bit images with enhanced contrast, rather than raw 16-bit images. Like the noise filters, this contrast enhancement is a black-box algorithm that likely has spatially varying and non-linear effects that are challenging to model. Therefore, thermal datasets with AGC enabled are also unsuitable for evaluating our method. Ultimately, we test our method exclusively on the TRNeRF dataset as it is the only dataset we are aware of that accounts for these concerns.

³Note that we are specifically referring to online noise filters, not static factory calibrated or shutter based corrections. The latter category of corrections does not violate the microbolometer camera model we adopt because they are constant offsets that are absorbed into the estimated FPN. Factory calibrated corrections were enabled in the TRNeRF dataset and shutter based NUCs were performed before each recording (but not during) [7].

H. Parameter Values

The full set of SLAM parameter values used for each sequence is given in Tab. 4. As explained in Sec. A.4, all spline control points are optimized with PyTorch’s `SparseAdam` optimizer. For the Gaussian and bias parameters the standard Adam optimizer is used.

For offline refinement, the image downsample factor is set to 1, the number of rasters per render is increased to 15, the integration interval is increased to 40 ms, the accelerometer residual loss coefficient is increased to 1×10^{-2} , the bias loss coefficient is set to 0, the bias learning rate is decreased to 1×10^{-4} , the opacity threshold is lowered to 0.005, the image plane gradient threshold is lowered to 2×10^{-4} , densification and pruning is performed every 250 iterations (up to the 4,000th iteration), and a global opacity reset is performed once at 3k iterations. The gravity direction is introduced as a learned parameter and it is optimized with the standard Adam optimizer using a learning rate of 1×10^{-4} . Offline refinement is run for a total of 15k iterations using a batch size of 10 renders.

I. Ablation Study

Our ablation study results are given in Tab. 5. Each method tested in the ablation study was run on each sequence for three trials. We report the number of trials completed and the average RMSE ATE across the completed trials (if any). Note that some trials are incomplete because our code exits when the entire rasterized alpha image at the current keyframe is beneath the threshold used for determining pixels to use in the median depth computation (0.95 in all of our experiments). This reliably indicates severe tracking failure that has placed the current camera view in a completely unmapped area.

Running our method without an IMU (i.e., in a pure monocular mode) fails on all but the slow sequences. On the SO sequence we observed that the initial estimate of the scene structure is skewed and that this results in a globally inconsistent trajectory. We found that using the gyroscope data immediately can be pivotal to the initial estimate of structure. As shown in the results, if the gyroscope data is not used before IMU initialization, performance is significantly harmed. The gyroscope data is in fact so useful that using the gyroscope data alone (without ever initializing the IMU) achieves great results on most sequences. However, without the accelerometer data to constrain it, there is sometimes a sudden irrecoverable jump in tracking error (something that could perhaps be addressed with a dynamics prior).

Running our method without modeling motion blur or rolling shutter (i.e., using a single raster per each render) performs surprisingly well on the MO and MI sequences, though it fails on the FO and FI sequences. The learned pixel-wise FPN seems to be one of the most essential components of

Table 4. SLAM parameter values.

Description	Value
Trajectory	
Spline order for the positions and rotations (k)	4
Knot interval for the positions and rotations (Δt_c)	~ 8 milliseconds (half the frame period)
Learning rates for the position and rotation control points	$1 \times 10^{-3}, 1 \times 10^{-4}$
Number of predicted poses used in spline fitting (N_q)	10 per knot in the time range of the predictions
IMU Parameters & Loss	
Learning rate for the gyro. and accel. biases	1×10^{-3}
Loss coefficients for the gyro. and accel. residuals (λ_g, λ_a)	$1 \times 10^{-2}, 1 \times 10^{-4}$
Loss coefficients for the gyro. and accel. residuals during relocalization (λ_g, λ_a)	$5 \times 10^{-4}, 5 \times 10^{-6}$
Loss coefficient for the gyro. and accel. biases (λ_{bias})	1×10^{-1}
Gaussians	
Initial Opacity	0.1
Learning rates for the opacities, intensities, means, scales, and quaternions	$5 \times 10^{-2}, 2.5 \times 10^{-3}, 1.6 \times 10^{-3}, 5 \times 10^{-3}, 1 \times 10^{-3}$
Rendering	
Image downsample factor	4
Number of rasters per render (N_r)	5
Maximum integration interval (T_b)	36 milliseconds
Spline order for the pixel-wise and scalar FPN components	2
Knot intervals for pixel-wise and scalar FPN components	30 seconds, 5 seconds
Learning rates for the pixel-wise and scalar FPN control points	$1 \times 10^{-4}, 1 \times 10^{-4}$
Loss coefficient for the pixel-wise FPN component (λ_{FPN})	1×10^{-3}
System Initialization	
Number of Gaussians created for map initialization (N_{init})	10k
Number of iterations for map initialization optimization ($N_{iter,init}$)	1k
Tracking & Keyframe Selection	
Maximum number of iterations for tracking optimization ($N_{iter,track}$)	100
Convergence thresholds for position and rotation	1×10^{-4} (relative scale), 1×10^{-4} radians
Alpha threshold used to determine valid pixels in median depth computation	0.95
Translation thresholds used in selecting new keyframes (min and max)	0.02, 0.07 (both normalized by the median depth in the current frame)
Intersection over union threshold used in selecting new keyframes	0.90
Keyframe window size ($ \mathcal{W}_K , N_{window}$)	6
Mapping	
Maximum number of Gaussians created for a new keyframe (N_{max})	5k
Alpha threshold used to determine candidate pixels for back projection in Gaussian creation	0.95
Candidate pixel fraction threshold, below which Gaussian creation is skipped	0.02
Number of iterations for mapping optimization ($N_{iter,map}$)	80
Number of randomly sampled keyframes ($ \mathcal{S}_K $)	4
Loss coefficients for the keyframe window and randomly sampled keyframes in mapping (λ_s, λ_w)	2, 0.33
Factor applied to the gradients of the position and rotation control points in the keyframe window	10
Relocalization SSIM threshold	0.92
Densification & Pruning	
Densification and pruning period	2k mapping iterations
Condition number threshold, above which Gaussian opacities are reset	8 (applied to the natural log of the condition number)
Opacity threshold, below which Gaussians are pruned	0.01
Image plane gradient threshold, above which Gaussians will be split or duplicated	4×10^{-4} (normalized, as described in Sec. E)
3D scale threshold, above which Gaussians are split and below which they are duplicated	0.01 (relative scale)
3D scale threshold, above which Gaussians are pruned	0.1 (relative scale)
IMU Initialization & Updates	
Time (since the first frame) at which to perform IMU initialization	10 seconds
Rate at which keyframe poses are sampled for use in IMU initialization and updates	2 Hz
Number of iterations for trajectory smoothing after IMU initialization	400
IMU update period	10 seconds
Warmup	
Delay before B-spline extension involves fitting to predicted poses	2 keyframes
Delay before motion blur and rolling shutter are modeled in rendering	20 keyframes
Delay before view-diversity-based opacity resetting is performed	40 keyframes
Delay before relocalization is enabled	150 keyframes

Table 5. Ablation study results.

Ablation Method	SO		MO		FO		SI		MI		FI	
	ATE (cm)	# of Trials Completed										
Monocular*	22.5	3	×	0	×	0	7.9	3	×	0	×	0
No Gyro. Before IMU Init.	51.8	3	32.6	1	18.0	3	10.2	3	8.3	3	×	0
Gyroscope Only*	3.6	3	5.7	3	3.7	3	3.3	3	4.6	1	×	0
No Roll/Blur Modeling	9.0	3	7.3	3	32.8	1	4.2	3	5.7	3	×	0
No Pixel-wise FPN	22.7	3	×	0	×	0	52.1	1	×	0	×	0
No Keyframe Weighting	9.0	3	91.8	3	3.3	3	4.0	3	×	0	×	0
No Opacity Resetting	14.6	3	12.8	2	3.5	3	6.6	3	9.4	3	×	0
No Relocalization	12.3	3	4.8	1	2.3	3	6.6	3	3.9	2	×	0
With Onboard Filters	14.0	3	4.2	3	2.4	3	3.7	3	×	0	×	0
TRGS-SLAM	12.7	3	5.5	3	2.4	3	6.4	3	3.9	3	4.2	3

* Poses are relative scale and Sim(3) alignment is used in evaluation.

× No trials were successfully completed.

our method, as disabling it yields failure in most sequences and poor results in others. Keyframe weighting in mapping, view-diversity-based opacity resetting, and relocalization are important in some sequences, but not all. However, the view-diversity-based opacity resetting significantly reduces the number of Gaussians, even when it isn’t pivotal to accurate tracking (e.g., in the fast outdoor sequence the final number of Gaussians is $\sim 34k$ with view-diversity-based opacity resetting and $\sim 120k$ without).

The last method in the ablation study, ”With Onboard Filters”, corresponds to running our method on the second FLIR ADK camera in the TRNeRF dataset, which had onboard noise filters enabled. The noise filters have no apparent impact on performance in the outdoor sequences where FPN is less prominent. In the indoor sequences they have an inconsistent effect. Our method runs without issue on the SI sequence. However, on the MI and FI sequences our method fails *immediately*. Note that all sequences begin with medium speed motion intended to aid IMU initialization, so the difference in performance between the SI and MI/FI sequences is not explained by their different camera speeds later in the sequences. This appears to suggest that these filters can enter a state in which they introduce significant multi-view inconsistency that violates the precise camera modeling our method relies on. As these filters are enabled by default, this may have implications to many thermal datasets collected with the same or similar cameras.

Finally, we note that only our full proposed method is able to succeed on the FI sequence.

J. Additional Timing Analysis

Table 6 gives a breakdown of timing in the MI sequence. Note that the timing data is presented hierarchically, with the indentation of the task names used to represent their parent-child relationships. Tracking runs for all 9654 frames, while mapping runs for each of the 2111 frames selected as keyframes (after system initialization). Mapping takes much longer to run than tracking, and consumes the most

time overall. Within tracking, B-spline extension consumes a modest percentage of the computation time, but the bulk of the time is spent in the optimization loop. In mapping, the optimization loop completely dominates. Optimization runs for an average of 32 iterations in tracking and 83 iterations in mapping. Note that mapping is typically run for exactly 80 iterations, but is occasionally run for more when densification and pruning occurs and the iteration counter is reset. The computation time is spread quite evenly across the individual components of the optimization loops in both tracking and mapping, so there are no clear bottlenecks.

K. Limitations

While our method demonstrates a unique capability to operate on the challenging TRNeRF dataset [7], it also has several limitations. Our random keyframe sampling scheme assumes a small scale scene, such that the randomly sampled keyframes will often have fields of view that overlap with the keyframe window. Similarly, our relocalization approach assumes a limited amount of drift, such that tracking is able to converge to the correct solution. These limitations could potentially be addressed by creating multiple submaps in large scale scenes, restricting the random sampling to the current submap, and performing place recognition and loop closure between submaps (similar to LoopSplat [63]). Additionally, in our testing we rescaled the 16-bit thermal images with hardcoded thresholds. In real online operation good thresholds are unlikely to be known apriori. This could be addressed by dynamically setting these thresholds and correspondingly making dynamic adjustments to the Gaussians’ intensities and the learned FPN estimates. Also, in our current implementation the IMU biases are assumed constant. For long-term operation the biases would be better represented as slowly varying splines, similar to our implementation of FPN.

Additionally, our method is sensitive to features commonly enabled in thermal cameras, such as onboard noise filters and AGC. This is not an issue if these features are dis-

Table 6. Timing analysis on the MI sequence.

Task	Avg. Time Per Run (ms) × Avg. Number of Runs per Parent Task	% of Parent Task
Tracking	193.27×9654	36.9
B-Spline Extension	27.32	14.1
Optimization Iteration	5.12×32	84.8
Rendering	1.88	36.8
Pose Evaluation	0.60	31.7
Rasterization	0.57	30.1
Blending & FPN	0.67	35.3
Loss Computation	0.75	14.3
Image Loss	0.08	11.0
IMU Loss	0.64	84.4
Backward Pass	1.22	23.1
Trajectory Optimizer Updates	1.05	19.9
Mapping	1469.39×2111	61.3
Gaussian Creation	0.63	0.04
Optimization Iteration	17.55×83	99.5
Rendering	3.06	17.4
Pose Evaluation	0.64	20.9
Rasterization	1.63	53.4
Blending & FPN	0.73	24.0
Loss Computation	1.56	8.9
Image Loss	0.20	12.9
FPN Loss	0.35	22.7
IMU Loss	0.98	63.2
Backward Pass	4.92	28.1
Gradient Modification	1.49	8.5
Optimizer Updates	2.90	16.5
Gaussian Updates	0.72	24.8
FPN Updates	0.81	27.9
Trajectory Updates	1.35	46.7
Densification	2.90	16.5

abled, but it does pose a potential issue with existing datasets that had these features enabled or with thermal cameras that do not expose the option to disable them. This issue could be potentially addressed by expanding the image formation model assumed by our method to incorporate these effects. Similarly, our method does not have a strategy for dealing with shutter-based NUCs, which both interrupt the image stream and cause abrupt changes to onboard FPN corrections. However, as mentioned in Sec. 5, it would be interesting to see if our method of estimating FPN could obviate the need for shutter-based NUCs in long-term operation. Finally, we note that these issues could also be mitigated on the manufacturer’s side: if the cameras report the necessary metadata to fully reconstruct the image processing pipeline (e.g., NUC tables) these onboard operations would no longer be sources of uncertainty in camera modeling.